J. Fluid Mech. (2011), *vol.* 679, *pp.* 1–31. © Cambridge University Press 2011
doi:10.1017/jfm.2011.77

Numerical study of flow through and around a circular array of cylinders

A. NICOLLE† AND I. EAMES

University College London, Torrington Place, London WC1E 7JE, UK

(Received 7 February 2010; revised 5 November 2010; accepted 10 February 2011; first published online 27 May 2011)

This paper describes a study of the local and global effect of an isolated group of cylinders on an incident uniform flow. Using high resolution two-dimensional computations, we analysed the flow through and around a localised circular array of cylinders, where the ratio of array diameter (D_G) to cylinder diameter (D) is 21. The number of cylinders varied from $N_C = 7$ to 133, and they were arranged in a series of concentric rings to allow even distribution within the array with an average void fraction $\phi = N_C(D/D_G)^2$, which varied from 0.016 to 0.30. The characteristic Reynolds number of the array was $Re_G = 2100$. A range of diagnostic tools were applied, including the lift/drag forces on each cylinder (and the whole array), Eulerian and Lagrangian average velocity within the array, and the decay of maximum vorticity with distance downstream. To interpret the flow field, we used vorticity and the dimensionless form of the second invariant of the velocity gradient tensor. A mathematical model, based on representing the bodies as point forces, sources and dipoles, was applied to interpret the results. Three distinct flow regimes were identified. For low void fractions ($\phi < 0.05$), the cylinders have uncoupled individual wake patterns, where the vorticity is rapidly annihilated by wake intermingling downstream and the forces are similar to that of an isolated cylinder. At intermediate void fractions ($0.05 < \phi < 0.15$), a shear layer is generated at the shoulders of the array and the force acting on the cylinders is steady. For high void fractions ($\phi > 0.15$), the array generates a wake in a similar way to a solid body of the same scale. For low void fraction arrays, the mathematical model provides a reasonable assessment of the forces on individual bodies within the array, the Eulerian mean velocity and the upstream velocity field. While it broadly captures the change in the rate of decay of the maximum vorticity magnitude Ω_{max} downstream, the magnitude is underpredicted.

Key words: computational methods, general fluid mechanics, wakes

1. Introduction

Within the context of industrial and environmental fluid mechanics, there are many common situations where localised groups of bodies are fixed in an incident flow, for example, offshore structures, shielded riser pipes, groups of islands or arrays of turbines in a wind farm. In these examples, the flow is inertially dominated, turbulent and unbounded. The bodies may have a complex geometrical form.

† Email address for correspondence: a.nicolle@ucl.ac.uk

https://doi.org/10.1017/jfm.2011.77 Published online by Cambridge University Press

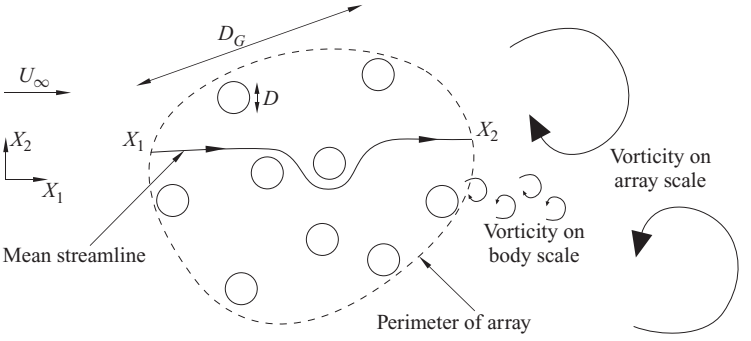

FIGURE 1. A schematic of a localised group of bodies in a uniform flow, along with the notation used in this paper.

The literature on bounded flow past multiple bodies is extensive, particularly in the context of heat exchangers. Far less research has been done on unbounded flows. The effect of boundedness is critical as it tends to increase the mean flow through groups of bodies, while for unbounded flows, the mean flow is decreased.

Most of the research on flow past groups of bodies has focused on the offshore industry where cylinders are most commonly used as constituent bodies – for instance as structural members. In the context of offshore risers, there are a number of experimental studies of the force on square groups, e.g. a (9×9) array of cylinders (Ball & Hall 1980). Much of this research was concerned with the forces on the group but Pearcey *et al.* (1982) also carried out measurements on the individual cylinders forming a square group (of 3×3). Ball & Hall (1980) investigated larger square arrays of cylinders of up to 9×9 for different angles, but only related this to the total group drag. Both studies were undertaken in a wind tunnel but did not characterise the flow field.

The number of bodies which forms the group is denoted by N_C as illustrated in figure 1. Some numerical studies have examined flow past groups of bodies, usually comprising a small number ($N_C < 10$), with attention usually paid to the structure of the flow. Chang, Yang & Chu (2008) applied Howe's decomposition method to look at how the flow signature from one cylinder affects downstream cylinders. A few theoretical studies have considered localised fixed arrays of bodies within a uniform flow, with most of the research limited to inviscid descriptions, such as Eames, Hunt & Belcher (2004). Eames *et al.* (2004) analysed the mean properties of the flow of an arbitrary shaped array, particularly the differences between Eulerian and Lagrangian methods of averaging. One of the important issues concerning groups of bodies is how the vortical flow signature from each body interacts and develops downstream. Hunt & Eames (2002) examined vorticity annihilation due to wake interactions and straining which suppresses far field flows. Moulinec, Hunt & Nieuwstadt (2004) examined these processes numerically for periodic cylinder flows and confirmed a rapid decrease in downstream vorticity maximum, which they interpreted as arising from straining in the wake.

As the number of bodies (N_C) within the array increases, the group begins to resemble a porous medium. At this limit, it becomes less important to fully resolve the flow around individual bodies whose effect on the ambient fluid can be represented in terms of a distributed drag force. This approach is well known, particularly for environmental flows, and has been applied by Taylor (1991).

https://doi.org/10.1017/jfm.2011.77 Published online by Cambridge University Press

One must, however, conclude from a review of the literature that there is a significant gap in studies of flows through and around localised groups of bodies. Previous numerical studies have been limited to examining the wake structures of small numbers of bodies fixed in a limited domain, while published experimental work has focused on the array/cylinder forces but not the flow. At a fundamental level, we need to better understand the effect of varying N_C on the flow through and around the group, and this, in turn, relates to the individual and collective wake structures and force contributions from the bodies. To simultaneously capture forces and flow field information for a large number of bodies in a uniform stream, we apply numerical calculations of sufficient resolution that both the local and downstream flows are fully resolved.

To allow fundamental analysis of this type of problem, accurate numerical results are important which implicitly limits the applicability of this research to practical engineering applications. Unlike the previously highlighted cases, which are three-dimensional and relatively high Re, we focus here on two-dimensional flow past a group of cylinders and limit our attention to when the local Reynolds number, characterised by a constituent cylinder, is sufficiently high to generate a characteristic von Kármán vortex street, whilst low enough to still be considered to be a two-dimensional flow. The onset of three-dimensional flow characteristics might well be anticipated due to the early triggering of three-dimensional vortices as a result of the complex two-dimensional geometry. The limitations of this two-dimensional approach are discussed in the conclusion § 6. To provide a means of evaluating and understanding the numerical results, we develop a point force model that enables the flow through and around the groups to be estimated.

The paper is structured as follows: in § 2, the numerical formulation and the cases that are considered are described. The diagnostics which are applied to the data sets are described in § 3. A point force model is discussed and developed in § 4 and applied to interpret the numerical results in § 5. The general conclusions are discussed in § 6.

2. Numerical formulation

The purpose of the numerical study was to analyse the effect of void fraction ϕ on the flow through and around a localised group of bodies and the forces acting on them. This is shown schematically in figure 1. The choice of the cylinder array configuration (of diameter D_G) in a uniform flow U_∞ is discussed in detail in § 2.1. The Reynolds number characterising the group $Re_G = D_G U_\infty/\nu$ was sufficiently high that vortex shedding occurred from individual cylinders at low void fractions.

The numerical study involved solving the Navier–Stokes and continuity equations,

$$\frac{\partial \boldsymbol{u}}{\partial t} + \boldsymbol{u}\cdot\nabla\boldsymbol{u} = -\frac{1}{\rho}\nabla p + \nu\nabla^2\boldsymbol{u}, \quad \nabla\cdot\boldsymbol{u} = 0, \tag{2.1}$$

where $\boldsymbol{u} = (u_1, u_2)$ is the velocity field, p is the pressure and ν is kinematic viscosity. The numerical technique is described in the Appendix. No-slip boundary conditions were applied to the rigid surfaces of the bodies; shear free conditions were applied to the bounding channel walls. On the inlet and outlet faces of the channel, the velocity $\boldsymbol{u} = (U_\infty, 0)$ and pressure $p = 0$ were, respectively, prescribed.

2.1. *Geometry*

The constituent components of the array were selected to be cylinders as they have well-understood flow characteristics (Zdravkovich 1997). The array was chosen to

https://doi.org/10.1017/jfm.2011.77 Published online by Cambridge University Press

Case	C_1	C_7	C_{20}	C_{39}	C_{64}	C_{95}	C_{133}	C_{S1}
N_C	1	7	20	39	64	95	133	1
ϕ	0.0023	0.0159	0.0454	0.0884	0.1451	0.2154	0.3016	1
Rows	0	1	2	3	4	5	6	NA
Nodes	3.29 m	3.73 m	3.76 m	3.76 m	3.76 m	3.75 m	3.74 m	3.34 m
Elements	6.58 m	7.48 m	7.54 m	7.53 m	7.55 m	7.54 m	7.53 m	6.68 m

TABLE 1. Description of cylinder arrays investigated and information about mesh quality.

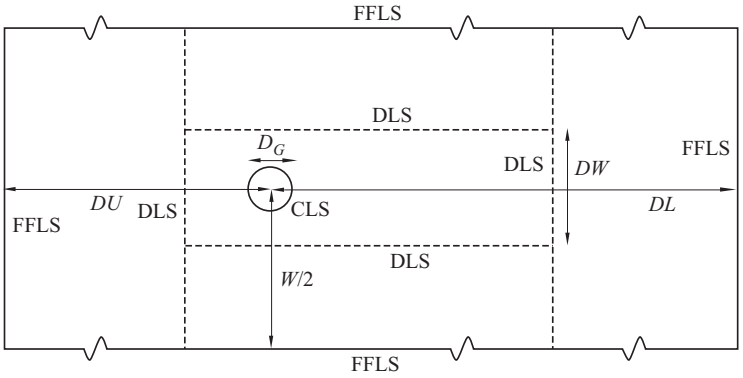

FIGURE 2. Schematic of the computational domain where the circle represents the edge of the cylindrical array. The inlet is on the left-hand side of the domain. The flow moves left to right in the figure.

have the same circular geometry as its constituent components so that, as the void fraction ϕ approached unity, the array became a solid cylinder. To enable the void fraction to be varied over a significant range, the diameter of the array D_G was chosen to be considerably larger than the diameter of the constituent components D. The number of cylinders in the array was $N_C = \phi(D_G/D)^2$, which varied from $N_C = 7$ to 133. The cases considered are labelled C_{N_C} except for $\phi = 1$, when we use the label C_{S1}. The characteristics for each case are tabulated in table 1.

The cylinders were arranged in concentric rings (starting from the circumference of the array) and filling inwards, with an additional cylinder at the centre. The cylinders were not distributed randomly as this could have an undue bias on the results, when N_C is small. The separation between the concentric rings and between the cylinders on each ring was the same. D_G was chosen to be $21D$ through the optimisation of the arrangements of cylinders in the arrays, which gave eight contrasting cylinder configurations consistent with the uniform spread within the array. For an isolated cylinder, $Re = DU_\infty/\nu$ was chosen to be 100, corresponding to a fully formed vortex street. This resulted in a Reynolds number for the array of $Re_G = 2100$.

The geometry and size of the outer computational domain is shown schematically in figure 2. To reduce the influence of the inlet, outlet and wall effects, the array was centred at a distance $DU = 950D$ from the inlet and on the centreline of the channel. The channel had a width $W = 500D$ and channel length from the centre of the group to the channel outlet of $DL = 2500D$. The array had a blocking ratio of $D_G/W = 0.042$, which is small enough that the correction to the force on the array was negligible (Blackburn 2006).

https://doi.org/10.1017/jfm.2011.77 Published online by Cambridge University Press

2.2. *Mesh specification*

As the focus of this work was to conduct an accurate but geometrically simplified numerical study using direct numerical simulation (DNS), particular care was taken in defining the mesh characteristic length scales. The mesh resolution was varied across the computational domain to optimise run time and take account of different wake length scales. A mesh independent study was conducted on a single cylinder, under similar flow conditions to those used in this numerical study. This anticipates the worst case scenario as bodies within a group will generally be subjected to a reduced flow field arising from blockage by the group.

The mesh independent study showed that, for the characteristic length scales used in this work, the errors in the current calculations (for an isolated cylinder) were no greater than 1.23 % and 0.08 % for lift and drag coefficients, respectively. A comparison was made with the test cases for the drag coefficient, Strouhal number and base pressure calculated by Codina *et al.* (2006), Nithiarasu & Zienkiewicz (2005), Ramon (2002), de Sampaio *et al.* (1993) and Malan, Lewis & Nithiarasu (2002). These are standard test cases for validating numerical schemes (Nicolle 2009).

The validation study identified the sensitivity of the Strouhal number to the resolution of the wake region. As a consequence of this, the resolution in the wake region was high, particularly behind individual bodies. The mesh elements had a characteristic face length of $0.02D$, $0.1D$ and $3.0D$ in the regions labelled CLS, DLS and FFLS, respectively (indicated in figure 2).

Adjacent to the surface of the cylinders, the boundary layer was resolved using a sub-region of fine elements, with a separate region making the transition to CLS. The boundary layer region thickness is $0.1D$ with a typical element length scale of $0.005D$, resulting in 20 elements across this region.

2.3. *Implementation*

The numerical simulations conducted were calculated using ACEfem. This code solves unstructured meshes, essential for complex geometries, such as those studied here. The meshes for the simulations were produced using Gmsh, written by Christophe Geuzaine and Jean-Francois Remacle, which was custom compiled using Intel compilers and 64-bit architecture.

ACEfem is a dynamic code which is formed from multiple modules. The code is highly parallelised and designed to run on cluster architectures, using the MPI protocol for communication. The numerical algorithms used PETSc version 2.3.3, produced by Argonne National Laboratories, with additional libraries Intel MKL 10.01 and hyper preconditioners produced by Sandia National Laboratories. Load balancing was achieved by distributing the mesh evenly amongst each of the processors using ParMETIS library. This minimises intercommunication amongst processors by reducing the number of edge cuts.

The calculations were carried out using a cluster formed of 640 nodes each having two Xeon dual core processors with 16 GB of memory and connected by a double data rate (DDR) low latency Infinipath network. Simulations were run using between 32 and 256 processors in an incremental fashion and utilised a quarter of a million processor hours. As a result of the large simulation size, post processing was required to be conducted in parallel using ACEfem. A core requirement of post processing was the ability to be able to interpolate values from the velocity field. This was achieved using a parallel data bin architecture, based on domain geometry, which reduced search time, especially when generating graphical figures and streamline plots. Data

https://doi.org/10.1017/jfm.2011.77 Published online by Cambridge University Press

were extracted from the simulations using a similar approach and saved in readable files for interpretation using plotting tools.

3. Diagnostics

A range of diagnostic tools was applied to analyse the data from the numerical simulations. These were defined at the outset and hard coded so that they were computed in real time on the supercomputer.

3.1. *Force diagnostics*

The cylinders within the array were labelled i, where $1 \leqslant i \leqslant N_C$. The force on the ith cylinder is defined by

$$\boldsymbol{F}_i = \int_{S_i} (p\boldsymbol{I} - \boldsymbol{\tau}) \cdot \hat{\boldsymbol{n}} \, \mathrm{d}S, \tag{3.1}$$

where $\boldsymbol{\tau}$ is the stress tensor, $\boldsymbol{I}$ is the identity matrix, S_i is the surface of the ith cylinder and $\hat{\boldsymbol{n}}$ is the unit normal into the cylinder (Batchelor 1967; Legendre, Borée & Magnaudet 1998). Drag and lift coefficients are usually defined in terms of an upwind, undisturbed free stream velocity. Since there are a large number of cylinders, the flow upwind of each cylinder is perturbed and, indeed, varied with time. Therefore, it is more relevant to define the lift and drag coefficients, in relation to the flow incident on the array $U_\infty \hat{\boldsymbol{x}}_1$. The drag and lift coefficients characterising the force on the ith cylinder are defined, in this paper, as

$$C_{Di}(t) = \frac{\boldsymbol{F}_i \cdot \hat{\boldsymbol{x}}_1}{\frac{1}{2}\rho D U_\infty^2}, \quad C_{Li}(t) = \frac{\boldsymbol{F}_i \cdot \hat{\boldsymbol{x}}_2}{\frac{1}{2}\rho D U_\infty^2}. \tag{3.2}$$

The time averaged drag coefficient for an individual cylinder over a period T from an initial time t_0 is defined by

$$\langle C_{Di} \rangle = \frac{1}{T} \int_{t_0}^{T+t_0} C_{Di} \, \mathrm{d}t. \tag{3.3}$$

For an individual body, the average maximum lift coefficient, $\langle C_{Li} \rangle_{max}$ was obtained by averaging the local maximum magnitude of the lift coefficient for each cycle in the period from t_0 to $T + t_0$.

The drag and lift coefficients of the array are defined as

$$C_{DG}(t) = \frac{\sum_{i=1}^{N_C} \boldsymbol{F}_i \cdot \hat{\boldsymbol{x}}_1}{\frac{1}{2}\rho U_\infty^2 D_G}, \qquad C_{LG}(t) = \frac{\sum_{i=1}^{N_C} \boldsymbol{F}_i \cdot \hat{\boldsymbol{x}}_2}{\frac{1}{2}\rho U_\infty^2 D_G}. \tag{3.4}$$

From (3.4), time averaged drag coefficient for the array is defined as

$$\langle C_{DG} \rangle = \frac{1}{T} \int_{t_0}^{T+t_0} C_{DG} \, \mathrm{d}t. \tag{3.5}$$

For the array, the average maximum lift coefficient, $\langle C_{LG} \rangle_{max}$ was obtained by averaging the maximum magnitude of the sum for each individual lift component of each cycle in the period from t_0 to $T + t_0$.

https://doi.org/10.1017/jfm.2011.77 Published online by Cambridge University Press

3.2. *Flow diagnostics*

To analyse the flow characteristics, a set of diagnostic tools was employed. The first technique was to analyse the distribution of the out-of-plane vorticity component $\omega = (\nabla \times \boldsymbol{u}) \cdot \hat{\boldsymbol{x}}_3$ within and downstream of the array. To distinguish between regions of the flow that were dominated by straining or rotation, we analysed the relative strength of the symmetric and non-symmetric components of the velocity gradient tensor defined by

$$\boldsymbol{\Sigma} = \tfrac{1}{2}(\nabla \boldsymbol{u} + (\nabla \boldsymbol{u})^{\mathrm{T}}), \quad \boldsymbol{\Omega} = \tfrac{1}{2}(\nabla \boldsymbol{u} - (\nabla \boldsymbol{u})^{\mathrm{T}}). \tag{3.6}$$

A usual measure of the magnitude of these tensors is $||\boldsymbol{\Sigma}||^2 = \Sigma_{ij}\Sigma_{ij}$ and $||\boldsymbol{\Omega}||^2 = \Omega_{ij}\Omega_{ij}$. Straining and vortical regions within a flow can be distinguished by calculating the second invariant of the velocity gradient tensor (Hunt, Wray & Moin 1988). We apply the dimensionless (second invariant of the velocity gradient tensor) measure,

$$E = \frac{||\boldsymbol{\Sigma}||^2 - ||\boldsymbol{\Omega}||^2}{||\boldsymbol{\Sigma}||^2 + ||\boldsymbol{\Omega}||^2}, \tag{3.7}$$

which is bounded between -1 and 1 (Davidson 2004) and takes the values of -1, 0 and 1 for vortical, shearing and irrotational flows, respectively. Equation (3.7) is a much more sensitive and precise indicator of whether fluid is irrotational rather than thresholding vorticity. While this measure has been applied to many turbulent flow studies (Jeong & Hussain 2006), it has not been widely applied to multi-body flows.

3.3. *Average Lagrangian and Eulerian velocity*

Due to the unsteady nature of the velocity field, it is useful to analyse the local flow in the array, using the time averaged velocity field defined as

$$\langle \boldsymbol{u} \rangle = \frac{1}{T} \int_{t_0}^{T+t_0} \boldsymbol{u} \, \mathrm{d}t. \tag{3.8}$$

The averaging period (T) was set on a case-by-case basis, taking into account both the eddy shedding cycle of the array and any additional cycles that affect the wake formation. The Eulerian averaged streamwise velocity is the spatial average of the velocity field over the array of bodies (Eames *et al.* 2004) and is defined as

$$\langle u_1 \rangle_E = \frac{1}{V_a(1-\phi)} \int_{V_a - V_b} \langle u_1 \rangle \, \mathrm{d}V, \tag{3.9}$$

where V_a is the volume/cross-sectional area of the array. This was calculated from the average velocity field within the circular perimeter formed around the array (of radius $D_G/2$).

The streamlines through the array were calculated by releasing N_p marked fluid elements (from x_{1k}, x_{2k}, where $k = 1, \ldots, N_p$) upstream of the array and integrating the coupled equations,

$$\frac{\mathrm{d}x_{1k}}{\mathrm{d}t} = \langle u_1 \rangle (x_{1k}, x_{2k}), \quad \frac{\mathrm{d}x_{2k}}{\mathrm{d}t} = \langle u_2 \rangle (x_{1k}, x_{2k}), \tag{3.10}$$

with respect to time. The history of the particle positions $(x_{1k}(t), x_{2k}(t))$ gives the streamline through the average velocity field. The second piece of information which is tracked is the time it takes for the fluid elements to be advected through the array (T_k), measured from when they are within a distance $D_G/2$ from the origin to when

https://doi.org/10.1017/jfm.2011.77 Published online by Cambridge University Press

they leave the array. In addition, the entry and exit points of the fluid elements are stored, providing the horizontal distance L_k. The fluid elements were released outside the array to prevent any local bias caused by their release in the boundary layer of the constituent cylinders.

The Lagrangian average horizontal velocity of a fluid element is L_k/T_k. The average Lagrangian streamwise velocity in the array is defined by

$$\langle u_1 \rangle_L = \left\langle \frac{L_k}{T_k} \right\rangle, \tag{3.11}$$

where the average is taken over the fluid elements which enter the array (Eames *et al.* 2004).

4. Mathematical model

A mathematical model was developed to provide a framework to interpret the numerical results. The basis of the model is a linear superposition of the effect of blocking, drag and downstream velocity deficit on the ambient flow. Since there are no dynamics in this model, the flow field is steady. The drag on the individual bodies (and their dipole moments) was obtained from a consistent closed application of the model itself.

4.1. *Flow field*

The steady flow past an isolated body, located at the origin, can be modelled (for laminar wakes) by summing the contributions from the incident uniform flow, dipole (blocking component), monopole (wake source component) and the wake deficit,

$$\boldsymbol{u}(x_1, x_2) = \underbrace{U_\infty(1,0)\hat{\boldsymbol{x}}_1}_{\text{uniform}} + \underbrace{\frac{Q(x_1,x_2)}{2\pi(x_1^2+x_2^2)}}_{\text{source}} + \underbrace{\frac{\mu}{2\pi}\frac{(-x_1^2+x_2^2,-2x_1x_2)}{(x_1^2+x_2^2)^2}}_{\text{dipole}} - \underbrace{(1,0)\mathrm{H}(x_1)\frac{Q}{\sqrt{4\pi\nu x_1/U_\infty}}\exp\left(\frac{-x_2^2U_\infty}{4\nu x_1}\right)\hat{\boldsymbol{x}}_1}_{\text{wake}}. \tag{4.1}$$

The above contributions are well known and described separately in Batchelor (1967). The wake component is weighted with the Heaviside step function, defined by $\mathrm{H}(x_1)=0$ for $x_1<0$ and 1 for $x_1>0$. For an unbounded flow, the average drag force on the body is related to the average momentum flux far downstream,

$$\langle F_D \rangle = \rho \int \langle u_1 \rangle (U_\infty - \langle u_1 \rangle)\,\mathrm{d}A = \rho U_\infty Q - \rho U_\infty \int (U_\infty - \langle u_1 \rangle)^2\,\mathrm{d}A, \tag{4.2}$$

where the integration is taken across a plane perpendicular to the upstream flow, and the downstream volume flux is

$$Q = \int (U_\infty - \langle u_1 \rangle)\,\mathrm{d}A. \tag{4.3}$$

For planar isolated bodies, where vortex shedding occurs, the velocity deficit in the wake is comparable to U_∞ and the second term in (4.2) may be important. When the downstream flow is laminar, for instance, created by wakes intermingling and cancelling, the velocity deficit is negligible and the second term in (4.2) is much

https://doi.org/10.1017/jfm.2011.77 Published online by Cambridge University Press

smaller compared to the first term. Under these conditions, the volume flux in the wake is related to the average drag force through

$$Q = \frac{F_D}{\rho U_\infty} = \frac{1}{2}\langle C_D \rangle D U_\infty \tag{4.4}$$

(Batchelor 1967, equation (5.12.15)). Equation (4.4) is only valid far downstream where a body's wake has become laminar and the wake Reynolds number has reduced. For an isolated cylinder, the dipole moment is set to be equal to the inviscid value,

$$\mu = \tfrac{1}{2} U_\infty \pi D^2, \tag{4.5}$$

corresponding to a cylinder (e.g. from Batchelor 1967, equation (7.9)). Even with an attached wake, the dipole moment is largely unchanged (Hunt & Eames 2002).

A first order analysis can be obtained by summing up the contributions from the bodies located at (x_{1i},x_{2i}) $(i = 1, \ldots, N_C)$,

$$\begin{aligned}\boldsymbol{u}(x_1, x_2) = \underbrace{U_\infty(1,0)\hat{\boldsymbol{x}}_1}_{\text{uniform}} + \sum_{i=1}^{N_C} \Bigg(& \underbrace{\frac{Q_i(x - x_i, x_2 - x_{2i})}{2\pi((x_1 - x_{1i})^2 + (x_2 - x_{2i})^2)}}_{\text{source}} \\ & + \underbrace{\frac{\mu_i}{2\pi} \frac{(-(x_1 - x_{1i})^2 + (x_2 - x_{2i})^2, -2(x_1 - x_{1i})(x_2 - x_{2i}))}{((x_1 - x_{1i})^2 + (x_2 - x_{2i})^2)^2}}_{\text{dipole}} \\ & - \underbrace{(1,0)\mathrm{H}(x - x_i) \frac{Q_i}{\sqrt{4\pi\nu(x_1 - x_{1i})/U_\infty}} \exp\left(\frac{-(x_2 - x_{2i})^2 U_\infty}{4\nu(x_1 - x_{1i})}\right) \hat{\boldsymbol{x}}_1}_{\text{wake}} \Bigg),\end{aligned} \tag{4.6}$$

where

$$Q_i = \tfrac{1}{2}\langle C_{Di} \rangle D U_\infty. \tag{4.7}$$

The monopolar contribution to the flow decays slowly with distance. The effect of a steady lift force is not accounted for in the above model because it decays much faster than the wake deficit created by the drag force. The effect of bounding channel walls in the numerical simulations has a negligible influence on the flow near to the array and on the downstream wake because $D_G/W = 0.042$. Within the group, the dipole moment is defined in terms of the local velocity past the cylinder,

$$\mu_i = \tfrac{1}{2} u_1(\boldsymbol{x}_i) \pi D^2, \tag{4.8}$$

where the velocity is calculated at the cylinder centre (when it is removed).

The model requires the drag coefficients (for (4.7)) and dipole moments (defined by (4.8)) on each body to be evaluated to close the problem. This was achieved using an iterative method where the ith cylinder was removed from (4.6) and the flow at $\boldsymbol{x}_i$ calculated. The semi-empirical drag law,

$$C_{T_i} = \begin{cases} 9.689 Re_i^{-0.78}\left(1 + 0.147 Re_i^{0.82}\right), & Re_i < 5, \\ 9.689 Re_i^{-0.78}\left(1 + 0.227 Re_i^{0.55}\right), & 5 < Re_i \leqslant 40, \\ 9.689 Re_i^{-0.78}\left(1 + 0.083 Re_i^{0.82}\right), & Re_i > 40 \end{cases} \tag{4.9}$$

https://doi.org/10.1017/jfm.2011.77 Published online by Cambridge University Press

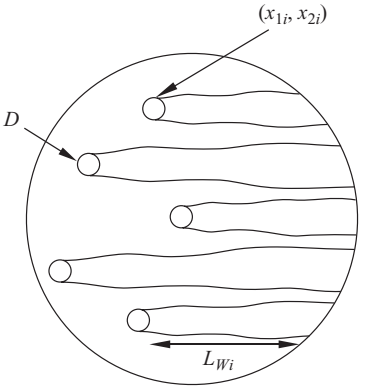

FIGURE 3. Schematic showing wake length in the array for an individual cylinder. The outer circle represents the edge of the array.

(taken from Clift, Grace & Weber 1978) was applied to estimate force on the ith cylinder, where $Re_i = |\boldsymbol{u}(\boldsymbol{x}_i)|D/\nu$. The drag coefficient corresponds to the component of the force on the cylinders, resolved in the streamwise direction and defined by $C_{Di} = C_{Ti}u_1(\boldsymbol{x}_i)/|\boldsymbol{u}(\boldsymbol{x}_i)|$.

The analytical model can be applied to analyse the effect of drag forces on the Eulerian mean velocity within the array. From (3.9), the Eulerian average velocity within the array is

$$V(1-\phi)\langle u_1\rangle_E - V(1-\phi)U_\infty = \int_{V-V_b} \left(\langle u_1\rangle - U_\infty\right)\,\mathrm{d}V. \tag{4.10}$$

The right-hand side of (4.10) describes the integral over the interstitial region within the array and this can be rewritten as the sum of the integrals over the wake and non-wake regions,

$$\int_{V-V_b} \left(\langle u_1\rangle - U_\infty\right)\,\mathrm{d}V = \int_{in\ wakes} (\langle u_1\rangle - U_\infty)\,\mathrm{d}V + \int_{outside\ wakes} \left(\langle u_1\rangle - U_\infty\right)\,\mathrm{d}V. \tag{4.11}$$

The contribution from the ith body to the integral over the wake region is

$$\int_{in\ wakes} (\langle u_1\rangle - U_\infty)\,\mathrm{d}V = -\int_0^{L_{Wi}} Q_i\,\mathrm{d}x_1. \tag{4.12}$$

The length of the wake of the ith body within the array is defined to be $L_{Wi} = \sqrt{D_G^2/4 + x_{2i}^2} - x_{1i}$ and is shown schematically in figure 3. The flow outside the individual wake regions is irrotational. The total contribution from the source flow terms is zero by cancellation between diametrically opposite cylinders within the array. Eames *et al.* (2004) showed that, for an inviscid dipolar flow past an array of cylinders in a circular array,

$$V(1-\phi)\langle u_1\rangle_E - V(1-\phi)U_\infty = 0. \tag{4.13}$$

Combining the above equations,

$$(1-\phi)\langle u_1\rangle_E - (1-\phi)U_\infty = -\frac{\displaystyle\sum_{i=1}^{N_C}\int_0^{L_{Wi}} Q_i\,\mathrm{d}x_1}{V}. \tag{4.14}$$

https://doi.org/10.1017/jfm.2011.77 Published online by Cambridge University Press

The term on the right-hand side was first identified in a study of interstitial velocity fields by Roig & Tournemine (2007, equation (4.7)) and Eames *et al.* (2007, equation (7.49)). From (4.1), Q_i is approximated as being constant along the wake length. An estimate of the Eulerian mean velocity within the array is

$$\frac{\langle u_1 \rangle_E}{U_\infty} = \frac{1 - \phi - \dfrac{\displaystyle\sum_{i=1}^{N_C} L_{Wi} Q_i}{V}}{1 - \phi}, \tag{4.15}$$

which can be evaluated using estimates of Q_i and the known cylinder positions. Equation (4.15) highlights the significant influence of viscous effects, exerting a drag on the bodies and reducing the Eulerian mean velocity. The expression (4.15) is also valid for flows past three-dimensional localised groups of bodies.

As we will see later, at low and intermediate void fractions the flow is characterised by wake intermingling and a dominant vortex is not shed from the array. In this regime, it is useful to apply a linearised vorticity equation to understand how the vortical flow signature decays downstream. This is estimated by adding together the contributions from all the bodies to give

$$\omega(x_1, x_2) = \sum_{i=1}^{N_C} \mathrm{H}(x_1 - x_{1i}) \frac{Q_i U_\infty (x_2 - x_{2i})}{2\nu(x_1 - x_{1i})} \left(\frac{U_\infty}{4\pi\nu(x_1 - x_{1i})} \right)^{1/2} \times \exp\left(-\frac{U_\infty (x_2 - x_{2i})^2}{4\nu(x - x_i)} \right). \tag{4.16}$$

The above expression for vorticity is consistent with the multibody flow model described by (4.6) and provides a means of interpreting the numerical results.

5. Numerical results

5.1. *Forces acting on individual cylinders in the array*

Figure 4 shows force scatter plots for each array considered. The scatter plots give an indication of the magnitude and mean direction of the forces acting on each cylinder. The position and size of each cylinder is plotted in grey and the darker (red online) region radiating from the centre of each cylinder is the scatter of the dimensionless force. For comparison, a light grey (red online) line is plotted below each cylinder array to indicate a drag coefficient of unity.

Figure 4(*a*), corresponding to case C_7, shows a weakly interacting group of cylinders. The two upstream cylinders show force scatter plots similar to that of an isolated cylinder. This is expected, as the incident flow was unobstructed and uniform, and the closest cylinder downstream was $10D$ away. The downstream cylinders experience a drag force which is slightly smaller than for an isolated cylinder, but the lift force is much larger because they are sitting in the wakes of the two upstream cylinders.

For array C_{20} (see figure 4*b*), cylinders are closer together and the interactive forces are, therefore, stronger. Upstream cylinders experience a drag force similar to that of an isolated cylinder, but the lift force, while still relatively small, is determined by the position of the cylinders downstream. Cylinders located in the wake of other cylinders (i.e. across the middle of the array) experience larger drag and lift forces as a result of the accelerated flow induced between the upstream bodies. The cylinders are still far enough apart that vortex shedding occurs, even though this is strongly

https://doi.org/10.1017/jfm.2011.77 Published online by Cambridge University Press

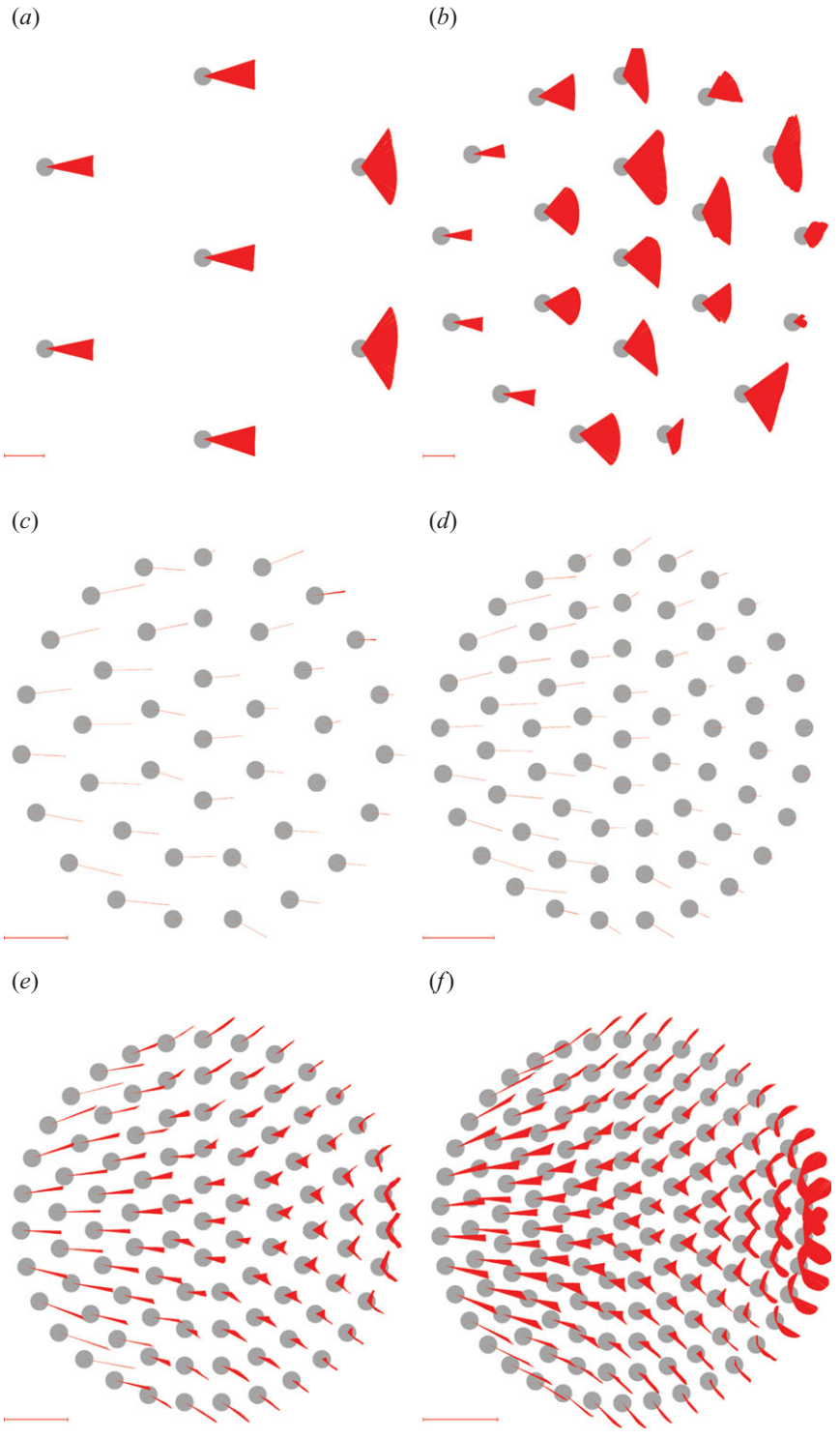

FIGURE 4. (Colour online) Force scatter plots for cases (*a*) C_7, (*b*) C_{20}, (*c*) C_{39}, (*d*) C_{64}, (*e*) C_{95} and (*f*) C_{133}. The light grey (red online) line below each plot shows unit force to enable comparison to be made between figures. The circles correspond to the cylinder positions, proportionately scaled. The flow is directed from left to right.

https://doi.org/10.1017/jfm.2011.77 Published online by Cambridge University Press

coupled in some cases. The forces experienced by the downstream cylinders are not symmetric because they are sensitive to the positions of upstream cylinders which are not symmetrically placed.

For arrays C_{39} and C_{64}, which have intermediate void fractions (see figures 4*c* and 4*d*), the force on the individual cylinders is steady and the lift force acting on the whole array is negligible. The aggregate drag force on the array is dominated by the contributions from the upstream rows of cylinders, which experience a drag force comparable to that of a single cylinder. The mean force on each cylinder is primarily streamwise, indicating that the flow is largely through the array, rather than around it.

For high void fractions, corresponding to C_{95} and C_{133} (figures 4*e*, 4*f*), the lift forces are significant and are mainly induced by the wake of the whole array. The mean force on the upstream cylinders has a cross-stream component, indicating that the flow diverges, as it passes through the front of the array. The reduction in the streamwise force on the upstream portion of the array is due to significant blocking by the array. The force scatter plots of the downstream cylinders have a butterfly-wing shape due to the influence of a recirculating wake which is being shed alternately from either side of the array.

The effect of increasing the void fraction (from C_{95} to C_{133}) leads to a slight increase in the scatter of the forces on the upstream cylinders and significantly increases the magnitude of the forces on the downstream cylinders. The scatter of the forces on the upstream cylinders increases because the wake is stronger and now has a greater influence on the flow past interior cylinders.

Figure 5 shows a comparison between model predictions (from (4.6)) and numerical calculations of the mean forces acting on the cylinders within the array. For all cases, the forces on the upstream cylinders are well predicted because the influence of downstream cylinders is not dependent on the details of the wake profile and only depends on the dipolar or monopolar contributions. For low void fractions, the agreement between the model and numerical calculations is good both in terms of the magnitude and direction of the mean force. For intermediate void fractions, the model is poor at predicting the magnitude of the forces on the cylinders sited at the sides of the array. This is because the modelling approach is based on the vortical signature of the wake being advected by the free-stream flow which cannot capture the shear layer around the edge of the array. For high void fractions, the mean force on most cylinders is well captured, except those at the sides of the array. The over-prediction of the forces on the third row of cylinders (in the higher void fraction cases) arises from the under-prediction of the initial individual wake width, so that these cylinders tend to see the free-stream flow, rather than sit in the wake of the upstream cylinders. Increasing the initial width of wakes improves the prediction of the cylinder drag but has a negligible effect on predictions of the collective array drag.

Figure 6 shows the variation of the average cylinder drag coefficient with void fraction. The average drag force decreases rapidly with void fraction (for $\phi < 0.2$) because, as the number of cylinders increases, the average flow within the array decreases (as shown by (4.14)). For higher void fractions ($0.2 < \phi < 0.4$), the mean flow through the array is weakly dependent on the void fraction, which also explains the weak dependence of the average drag force on ϕ in this region.

5.2. *Forces acting on the whole array*

Figure 7 shows the variation of the array drag and lift coefficients with time, with the corresponding average drag and lift coefficients plotted in figure 8. The array Strouhal

https://doi.org/10.1017/jfm.2011.77 Published online by Cambridge University Press

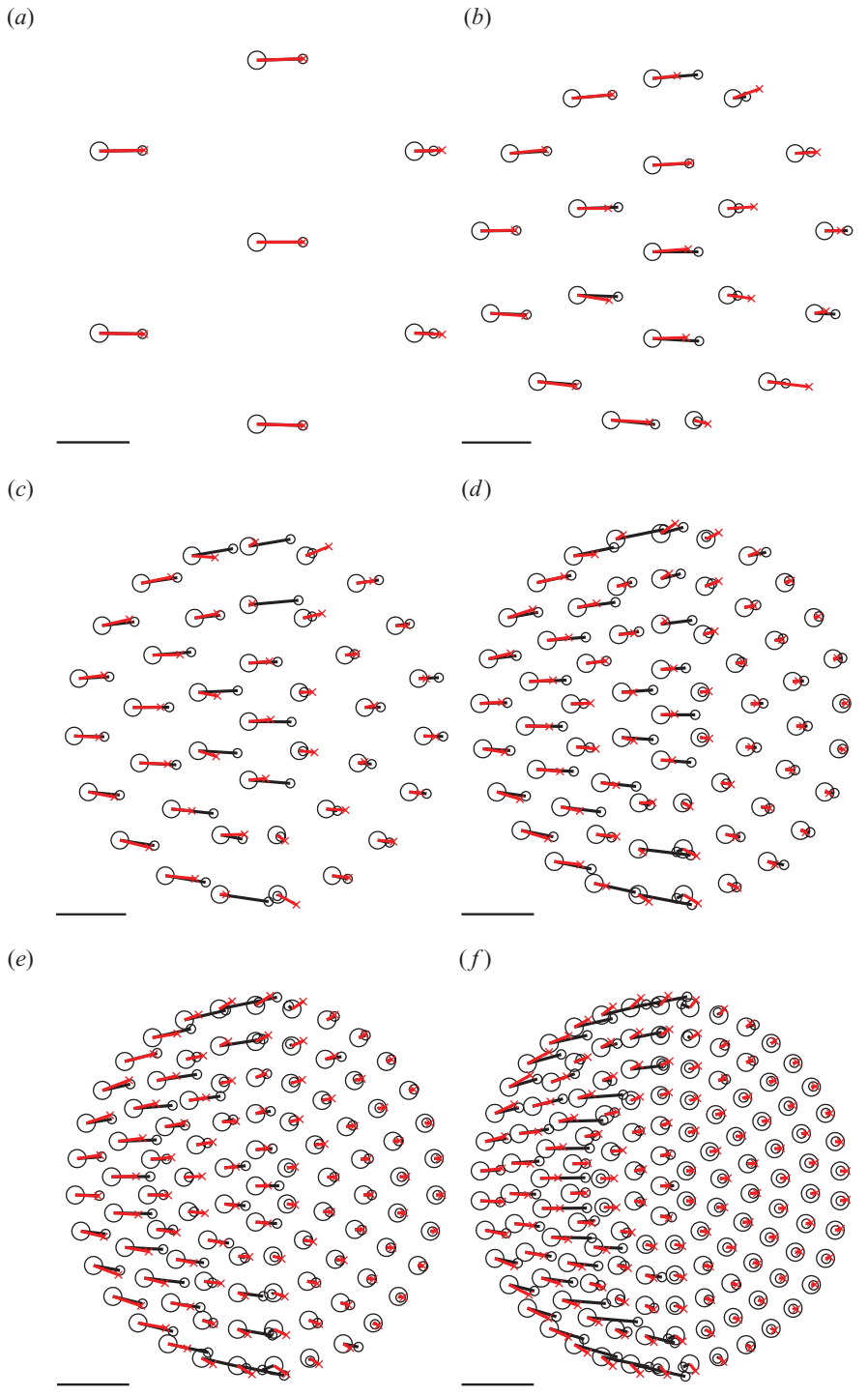

FIGURE 5. Comparison between the predicted mean force on cylinders within each array and the numerically evaluated force for (*a–f*) the same as for figure 4. The small symbols black (○) and red (×) correspond to the numerical and model predictions, respectively. The black line below each plot represents a unit of force which is the same for each figure. The circles correspond to the cylinder positions, proportionately scaled. The flow is directed from left to right.

https://doi.org/10.1017/jfm.2011.77 Published online by Cambridge University Press

Case	C_1	C_7	C_{20}	C_{39}	C_{64}	C_{95}	C_{133}	C_{S1}
$\langle C_{Di}\rangle = \dfrac{\langle C_{DG}\rangle}{N_C}$	0.0619	0.0530	0.0408	0.0249	0.0173	0.0173	0.0133	*
$\langle C_{DG}\rangle$	0.0619	0.3707	0.8155	0.9694	1.1063	1.6460	1.7678	1.6497
$\langle C_{Li}\rangle_{max}$	0.0145	0.0065	0.0079	0.0001	0.0000	0.0038	0.0055	*
$\langle C_{LG}\rangle_{max}$	0.0145	0.0453	0.1581	0.0006	0.0000	0.3604	0.7278	1.7353
$\langle St_G\rangle$	3.5503	3.3695	2.8897	1.1297	0.0000	0.2542	0.2547	0.2430

TABLE 2. Summary of the drag and lift coefficients and metrics for the cases investigated.

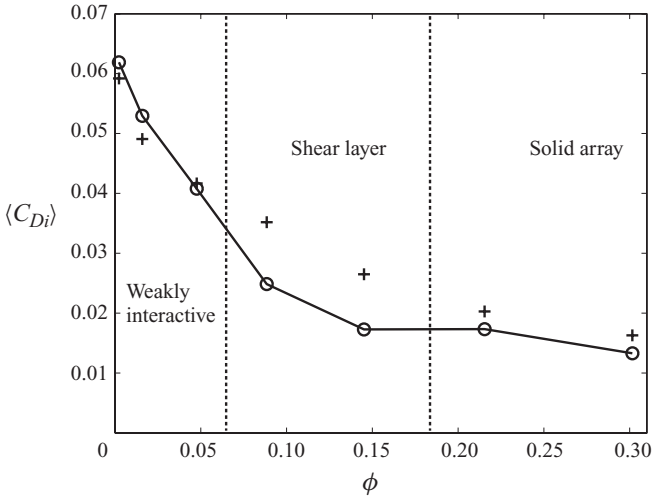

FIGURE 6. The variation of the average cylinder drag coefficient in the array, $\langle C_{Di}\rangle$ (defined by (3.3)) with ϕ plotted for both the numerical results (○) and predictions (+).

numbers, defined by $St_G = U_\infty T_p/D_G$, where T_p is the dominant period associated with the lift force, are listed in table 2.

For low void fractions (C_7 and C_{20}, see figure 7*a*), the wake shedding from the individual cylinders is generally in phase, leading to a Strouhal number of the array typical of an isolated cylinder (case C_1). This means that the array Strouhal number is estimated to be $St_G = (D/D_G)St \sim 3.55$, where $St = 0.169$ is the Strouhal number typical of an isolated cylinder. This estimate compares well with the data presented in table 2 for C_7 and C_{20}.

In C_{20}, the array lift coefficient is proportionately larger than that in C_7 (see figure 8*b*) resulting in a peak. While the array lift coefficient increases with ϕ, the average lift coefficients in C_7 and C_{20} are comparable (table 2). This is explained as ϕ is small in these cases and individual body wakes still are comparable in magnitude to an isolated body. In addition, due to proximity to one another, these wakes become phase locked and thus, contribute to the lift with minimal cancellation. The array lift coefficient has a high St_G indicative of phase locking of wakes shed by individual cylinders (see figure 7*b*). On top of this, there is a modulation of C_{LG} at a low frequency (with St_G estimated to be 0.2) which is more typical of shedding from the array.

For intermediate void fractions (C_{39} and C_{64}), the lift coefficient on the entire array is small $< 10^{-4}$ (see figure 8*b* and therefore omitted from figure 7*b*) and the drag force

https://doi.org/10.1017/jfm.2011.77 Published online by Cambridge University Press

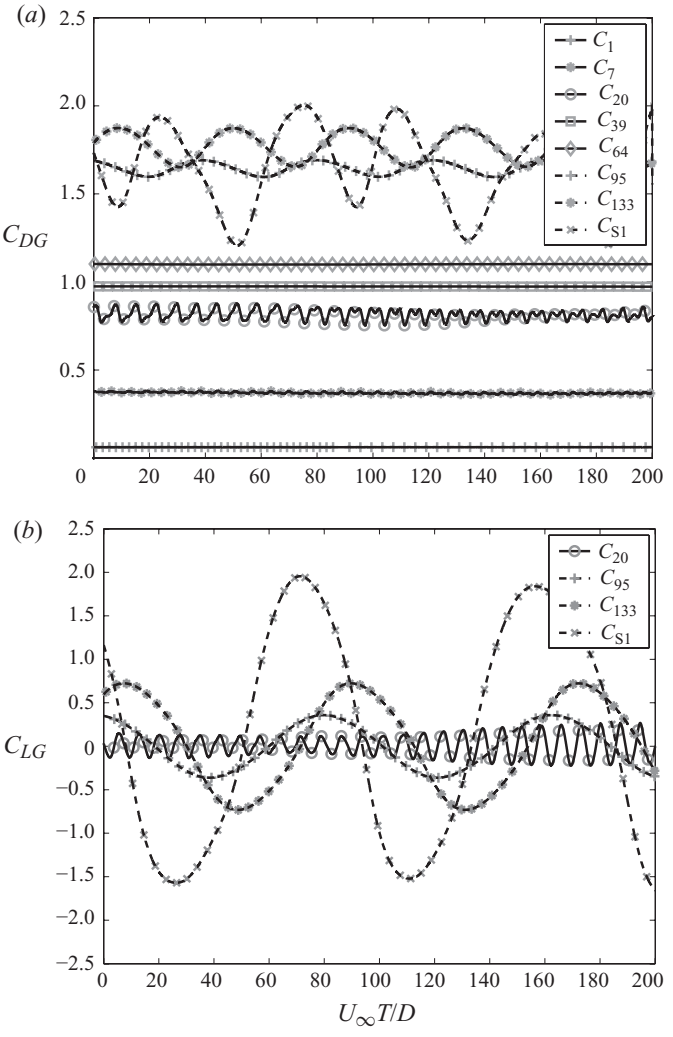

FIGURE 7. The time dependent array drag (C_{DG}) and lift (C_{LG}) coefficients (defined in (3.4)) are shown in (*a*) and (*b*) respectively. The legend in each figure shows the case presented.

is steady (figure 8*a*). The very small lift coefficient may arise from either the cylinders not being symmetrically placed or the group's wake being disturbed from downstream. The published research on flows past bluff porous bodies with base bleed have mainly focused on flat plates (Castro 1971; Huang, Kawall & Keffer 1996; Kim & Lee 2001). However, some work done by Bhattacharyya, Dhinakaran & Khalili (2006) and Yu *et al.* (2010) also studied numerically the flow past a porous cylinder and square, in two dimensions for low Reynolds number $Re < 40$, 50, respectively. This work mainly involved investigating industrial processes and, whilst these simulations were steady, they demonstrated how the trailing vortices were displaced downstream for a lower Darcy number. Castro (1971) studied the flow behind a porous plate and observed a critical void fraction $\phi \approx 0.2$, when the vortex street behind the plate disappeared because of the stabilising influence of base bleed. This is somewhat similar to what is seen in cases C_{32} and C_{64}. That value is higher than found in this work but as

https://doi.org/10.1017/jfm.2011.77 Published online by Cambridge University Press

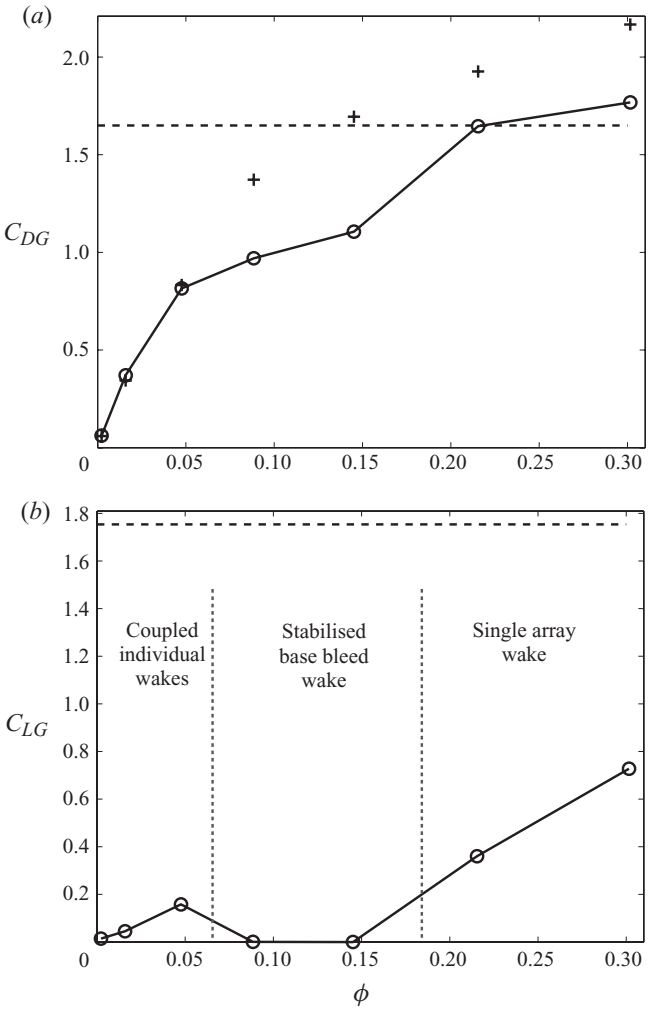

FIGURE 8. The array drag ($\langle C_{DG}\rangle$) and lift ($\langle C_{LG}\rangle_{max}$) coefficients are plotted in (a) and (b), respectively, as functions of void fraction (ϕ). The dashed line corresponds to the limit $\phi = 1$, while the symbols $\circ$ and $+$ correspond to numerical results and model predictions respectively.

pointed out in Huang *et al.* (1996), the wake behaviour depends on body shape and void fraction.

At high void fractions, (C_{95} and C_{133}), the wake pattern begins to exhibit properties similar to the wake of a solid cylinder C_{S1}. For both arrays, the lift coefficient is sinusoidal (figure 7b). The magnitude of the lift coefficient increases with ϕ towards the value seen in C_{S1} (figure 8b). However, neither exhibited the same instability that is seen in the lift coefficient in C_{S1}, where the magnitude of this fluctuated erratically by up to 50 %. This erratic behaviour is also evident in the drag force for C_{S1} shown in figure 7(a). This instability has been identified by Singh & Mittal (2004) who carried out highly resolved two-dimensional calculations at similar Reynolds numbers to case C_{S1}, investigating the two-dimensional effect on shear layer instabilities. The drag force on C_{95} and C_{133} fluctuates at twice the frequency of the lift force but with a regular amplitude. The erratic behaviour seen in C_{S1} is a feature of two-dimensional high Re cylinder flow and results from instabilities in the shear layer affecting separation of

https://doi.org/10.1017/jfm.2011.77 Published online by Cambridge University Press

the boundary layer on the wall. This behaviour possibly does not occur in C_{95} and C_{133} because of the absence of a rigid bounding wall.

In both C_{95} and C_{133}, the drag force is equivalent to or greater than that of case C_{S1}. This is believed to arise to some degree from the larger perimeter surface area of the array but mainly from the wider shedding angle of the detaching shear layer as can be seen clearly in figure 9. This effectively presents to the flow as a wider bluff body than that of case C_{S1} where the shedding angle is almost parallel to the flow.

5.3. *Flow diagnostics*

The flow is discussed with reference to the vorticity field and dimensionless second invariant of the velocity gradient tensor E. The instantaneous vorticity field is used to interpret the wake signatures in the near and far field as the time-averaged vorticity field tends to smear out important information about the structure of the flow, particularly the attached wakes.

For an isolated cylinder C_1 (figure 9*a*), positive and negative vorticity are shed alternately and are then advected downstream. The characteristic Reynolds number is $Re = 100$ and is sufficiently low that, within a distance of DRe, the discrete vortices evident in the near field have diffused into one another to generate a laminar planar wake characterised by adjacent strips of positive and negative vorticity, as shown in figure 10(*a*). Similar features are seen in C_7 and C_{20} (figure 9*b*, *c*) where vortices are shed from each cylinder and advected downstream in a region of width D_G. The individual vortices shed from each cylinder merge and rapidly cancel, broadly over the same distance as in C_1. Beyond a distance of $500D$, the vorticity appears to organise into coherent lumps of positive and negative vorticity, as seen in figure 10(*b*, *c*).

For intermediate void fractions (C_{39} and C_{64}), the vorticity field outside the array is characterised by two intense and stable vortex sheets (of opposite sign) (figure 9*d*, *e*). Beyond a critical distance downstream, the sheets are unstable and a von Kármán vortex street is created further downstream (figure 10*d*, *e*). The critical distance is determined by the bleed flow through the array, which decreases as ϕ decreases. While the vorticity created by the individual cylinders is intense, their vorticity signature does not survive as the flow passes through the array and is rapidly attenuated. This local mechanism is likely to be due to vorticity annihilation, caused by wake interactions (Hunt & Eames 2002).

For high void fractions (C_{95} and C_{133}, figure 9*f*, *g*), the detached shear layer becomes unstable close to the array. This results in a narrow region of intense vorticity behind the array, which dominates any vorticity generated within the array (in C_{95} and C_{133}). Far downstream (figure 10*f*, *g*), the positive and negative regions of vorticity are now widely separated and vorticity annihilation does not occur. The maximum magnitude of the vorticity decreases slowly with downstream distance, due to the diffusive growth of the vortical lumps. In both these cases, a clear and stable von Kármán vortex street is produced, which is similar to that of a solid cylinder. On the other hand, C_{S1} produces a vortex street (see figure 10*h*) which is not periodic, due to the sensitivity of the point of separation from a rigid wall at such a high Reynolds number.

The dimensionless measure of the second invariant of the velocity gradient tensor, E, enables vortical, shearing and irrotational regions to be discriminated. These are respectively coloured as blue, green and red in figure 11. Figure 11(*a*) shows case C_1, where the downstream vortex street is enclosed by a weak shear layer. A shear layer can also be seen extending from the shoulders of the cylinder. In figure 11(*b*) (case C_7), the void fraction is still sufficiently low that the wakes are well separated

https://doi.org/10.1017/jfm.2011.77 Published online by Cambridge University Press

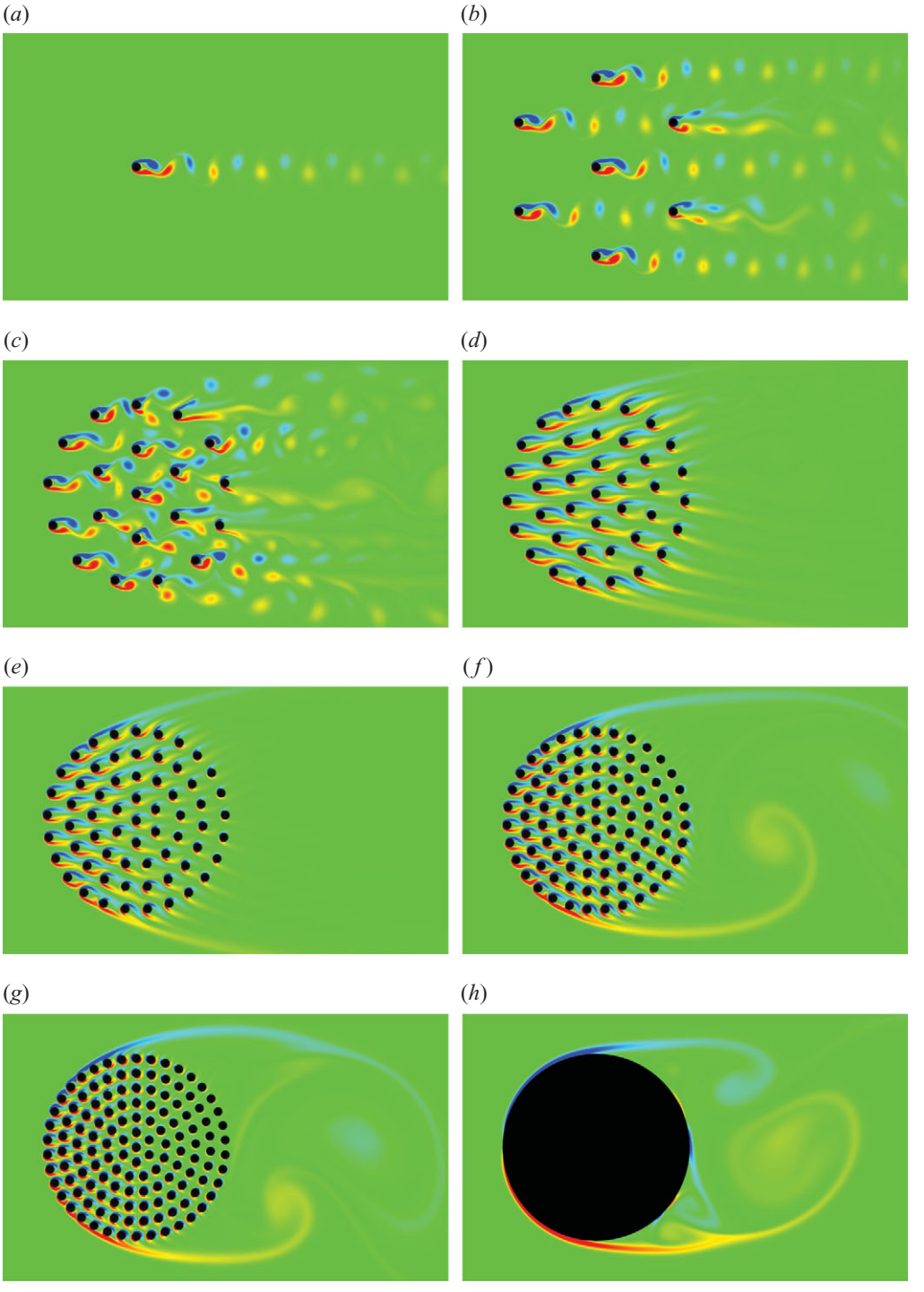

FIGURE 9. Near field view of the vorticity field, ω, for the arrays (*a*) C_1, (*b*) C_7, (*c*) C_{20}, (*d*) C_{39}, (*e*) C_{64}, (*f*) C_{95}, (*g*) C_{133} and (*h*) C_{S1}. The colours red and blue denote positive and negative vorticity respectively, with green corresponding to irrotational fluid. The flow is directed from left to right.

https://doi.org/10.1017/jfm.2011.77 Published online by Cambridge University Press

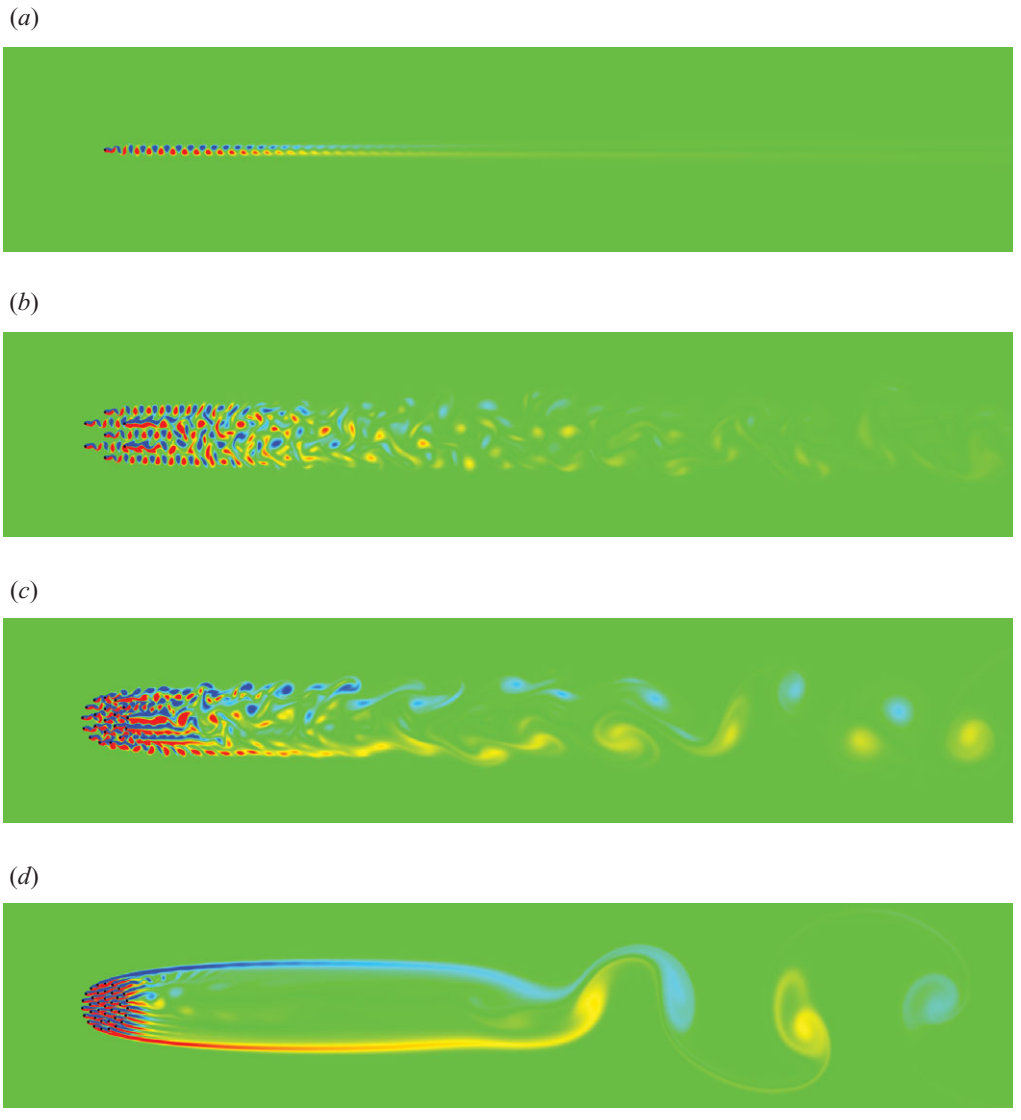

FIGURE 10. For caption see next page.

by irrotational fluid, until far downstream where the array wake is formed by low intensity vorticity. For higher void fractions (figure 11*c*, case C_{20}), the vorticity in the wake begins to be annihilated (at a distance of $2D_G$) downstream of the array, which is now characterised by large pockets of irrotational fluid.

Figure 11(*d*) shows the first case (C_{39}) in which the array wake is fully established. The flow is characterised by shear layers attached to the array, which are bounded by an intense vortex sheet. A remarkable feature of this case is the extent of the areas of vorticity and shear flow within the wake region, which can only be formed through annihilation and accumulation of vorticity. Within the array, thin dividing regions of irrotational flow form between the cylinders by a process of vorticity annihilation. Figure 11(*e*) (case C_{64}) shows similar features within the array. The entire wake attached to the array is bounded by a coherent, thin vortex street. The flow within the

https://doi.org/10.1017/jfm.2011.77 Published online by Cambridge University Press

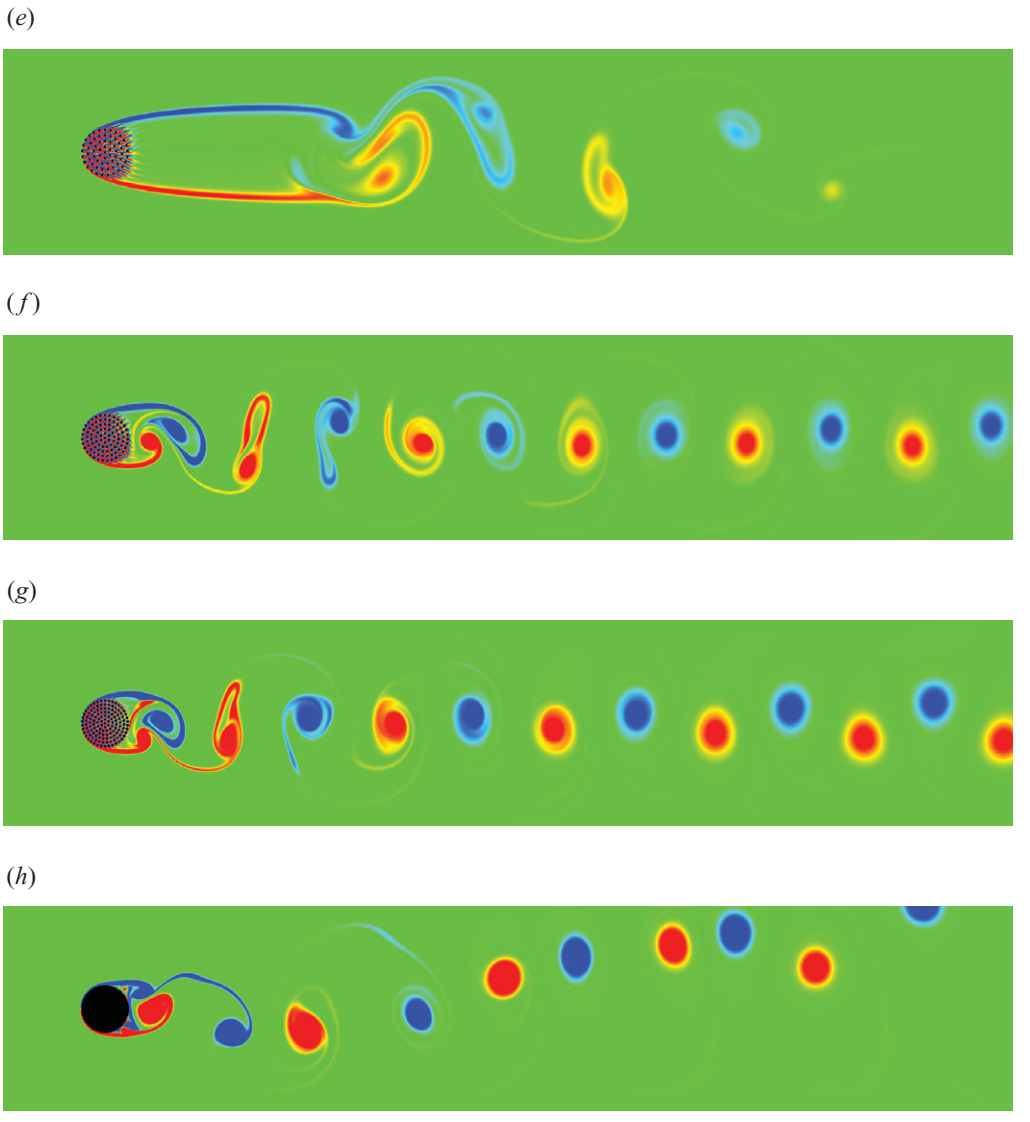

FIGURE 10. Far field view of the vorticity field, ω, for the arrays (*a*) C_1, (*b*) C_7, (*c*) C_{20}, (*d*) C_{39}, (*e*) C_{64}, (*f*) C_{95}, (*g*) C_{133} and (*h*) C_{S1}. The colours red and blue denote positive and negative vorticity respectively, with green corresponding to irrotational fluid. The flow is directed from left to right.

wake forms two counter-rotating shear flows shown in green, apart from an almost symmetrical, thin, irrotational, dividing region on the centreline. This indicates that there is uniform circulation within the wake, with a shear velocity gradient through this region of equal strength to the circulation. Downstream cylinders produce finger-like shear layers extending a distance $7D$ downstream which are bounded by a region where the flow is irrotational.

Cases C_{95} and C_{133} (figure 11*f*, *g*) can be viewed as typical of what would also be expected from a solid cylinder (case C_{S1}, figure 11*h*). The attached recirculating region behind these arrays entrains irrotational fluid, causing the isolated roll-up of

https://doi.org/10.1017/jfm.2011.77 Published online by Cambridge University Press

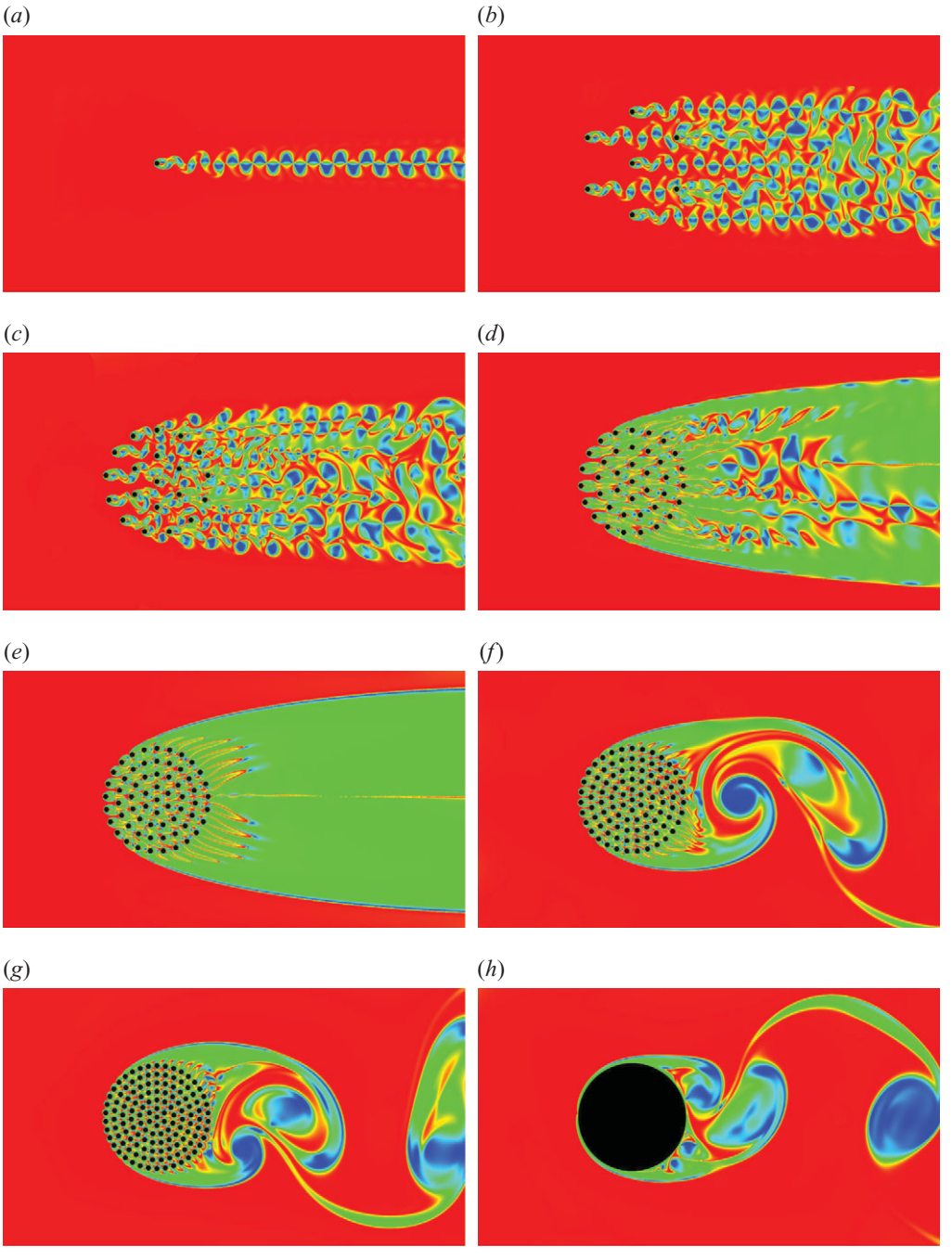

FIGURE 11. The dimensionless second variant of the velocity gradient tensor, E, (3.7) is plotted for the arrays (*a*) C_1, (*b*) C_7, (*c*) C_{20}, (*d*) C_{39}, (*e*) C_{64}, (*f*) C_{95}, (*g*) C_{133} and (*h*) C_{S1}. The colours red, blue and green correspond to $E = -1, 1, 0$ and relate to irrotational, vortical and shearing motions. The flow is directed from left to right.

intensive vortex sheets, which are advected downstream. The flow signature from the individual cylinders, for C_{95} and C_{133}, are engulfed into the wake of the array and quickly dissipated. From the shoulders of the arrays, a shear layer separates

https://doi.org/10.1017/jfm.2011.77 Published online by Cambridge University Press

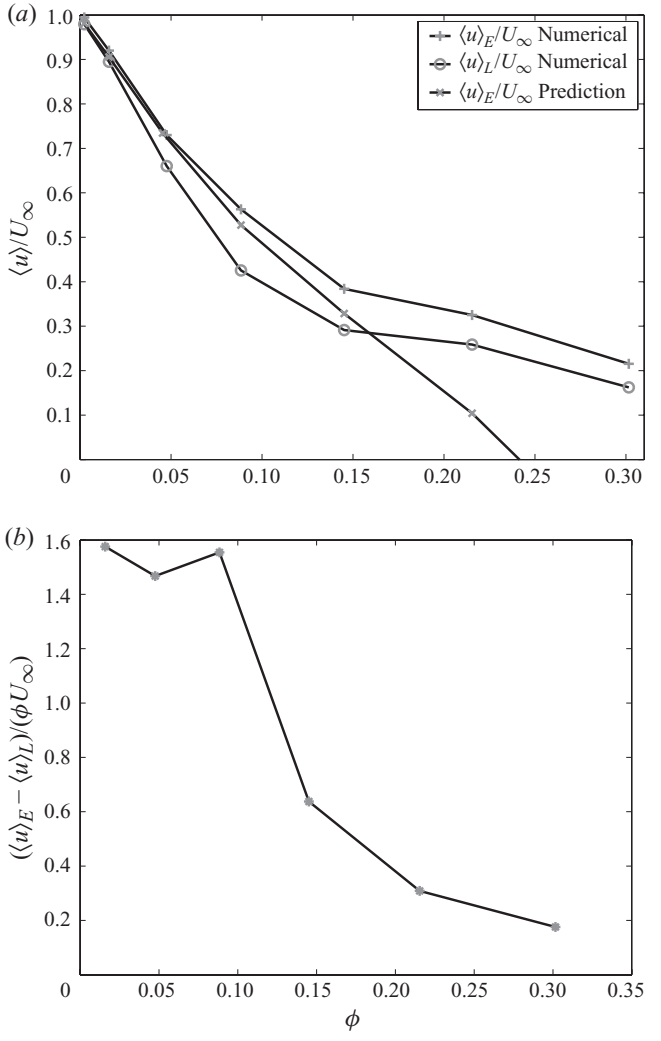

FIGURE 12. Variation of (*a*) Eulerian (+) and Lagrangian (○) average velocities with void fraction and (*b*) the difference between the Eulerian and Lagrangian average velocities with void fraction. In (*a*) the prediction (4.15) is plotted as (×).

which creates the vortex street downstream. The vortices are separated by a shear layer.

5.4. *Lagrangian and Eulerian average velocities*

Figure 12(*a*) shows the variation of the Eulerian and Lagrangian averaged streamwise velocities as a function of void fraction and contrasts the numerical calculations with the model prediction (4.15). The agreement between the predictions of $\langle u\rangle_E$ and the numerical results is good for $\phi < 0.15$. The multipole model is based on low void fractions where the wake width is zero at x_i which means, for close body spacing, that the velocity deficit is over predicted. This explains why the mean flow is lower than the results for the full numerical calculations. The conclusion is that the mean flow is largely dominated by the wakes which tend to reduce the flow between the bodies and this effect is larger than the inviscid kinematic effect of the bodies blocking the flow.

https://doi.org/10.1017/jfm.2011.77 Published online by Cambridge University Press

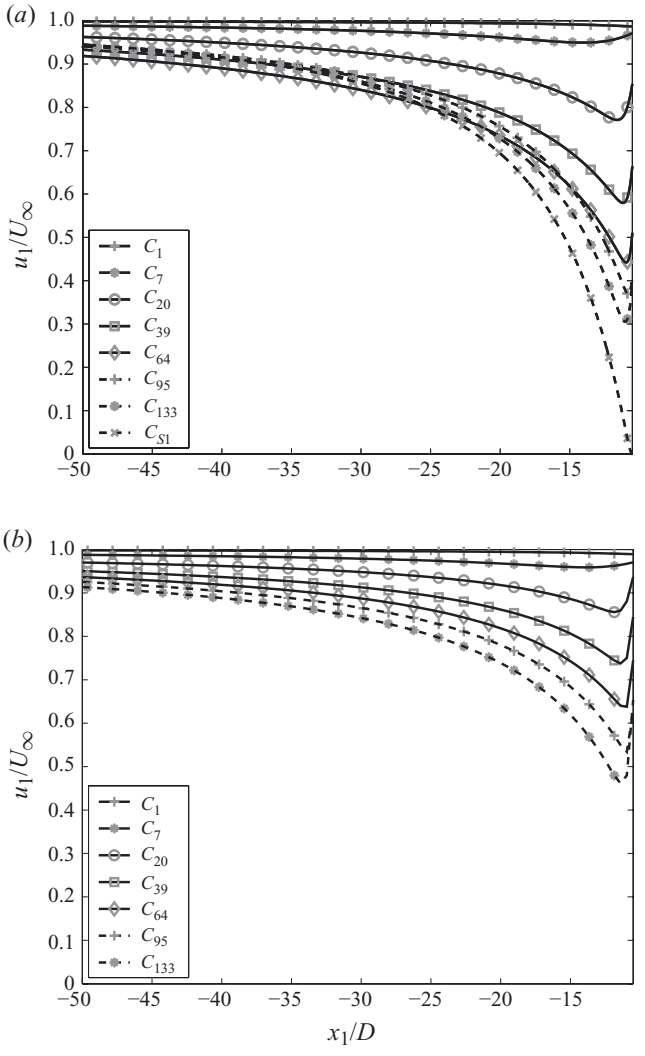

FIGURE 13. Variation of centreline velocity with distance upstream of the array for contrasting void fractions. The key indicates the number of cylinders in the array. Numerical and predicted profiles are plotted in (*a*) and (*b*), respectively.

The Eulerian and Lagrangian averaged velocities in the array depend on the shape of the array and give different assessments of the flow field. An inviscid analysis by Eames *et al.* (2004) predicts this difference to be 1.0ϕ, which is close to the calculated value 1.5ϕ reported in figure 12(*b*). For low void fractions, the difference between the Lagrangian, Eulerian and predictions is small.

5.5. *Upstream velocity perturbation*

Figure 13 shows the centreline streamwise velocity (u_1), upstream of the array, for varying void fractions. The flow is irrotational and slows down, due to the blocking effect of the entire array and the drag force from the bodies. Within a distance $\sim D$ of the front of the array, the flow is influenced by the placement of individual cylinders. For case C_{S1}, the flow is completely blocked at $x = -D_G/2$, as a consequence of the kinematic condition applied on the surface of the cylinder. Comparison between the

https://doi.org/10.1017/jfm.2011.77 Published online by Cambridge University Press

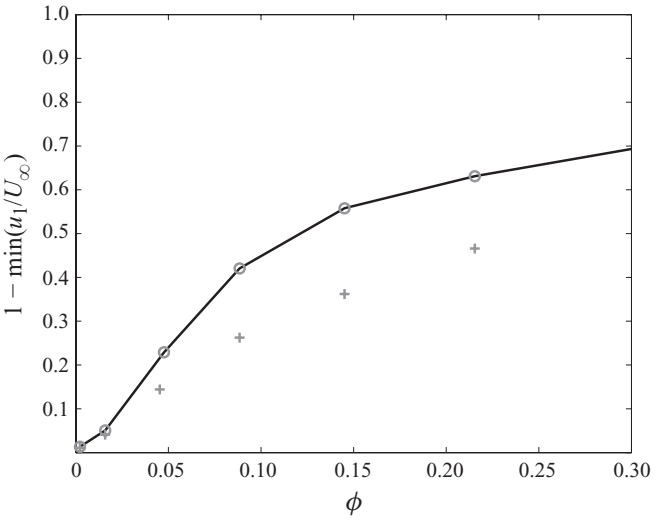

FIGURE 14. Variation of the minimum upstream centreline velocity as a function of void fraction. The symbols correspond to numerical calculations (○) and predictions (+) from (4.6).

numerical calculations and model predictions (figure 13*a*, *b*, respectively) shows good agreement.

A detailed comparison is made by comparing the centreline velocity at the edge of the array (figure 14). The model gives a good prediction for $\phi < 0.15$. The discrepancy seen between the numerical and model results, for high ϕ and for the solid cylinder (C_{S1}), is due to the model being a point force and dipolar representation, which is valid only for well-separated cylinders.

5.6. *Vorticity decay within the wake*

The decay of the vorticity maximum, defined as $\Omega_{max}(x_1) = \max_{-w < x_2 < w} |\omega(x_1, x_2)|$, with distance downstream from the array, provides an indication of the structure of the vorticity in the wake, particularly the separation of the positive and negative components of vorticity. The variation of Ω_{max} with downstream distance is shown in figure 15, for distances beyond the edge of the array. The two main processes which lead to Ω_{max} decreasing with downstream distance are (*a*) diffusion which causes Ω_{max} to decay as $x_1^{-1/2}$ and (*b*) vorticity annihilation caused by positive and negative vorticity intermingling causing Ω_{max} to decay rapidly as x_1^{-1}.

Adjacent to the sides of the array, a steady shear layer is created, corresponding to vorticity of one sign. Along these shear layers, the vorticity spreads in the same manner as a passive contaminant leading to a $x_1^{-1/2}$ decay. However, the vorticity field behind an isolated body is characterised by a bipolar source (corresponding to the cross-product of the point force action of the body), with the combined action of vorticity annihilation and diffusion leading to a faster x_1^{-1} decay (e.g. see (4.16)).

To enable the numerical results to be interpreted, figure 15 includes two lines with gradients $-1/2$ and -1. Figure 15(*a*) shows the decay of Ω_{max} with downstream distance for C_1, C_7 and C_{20}. The low Reynolds number ($Re = 100$) for case C_1, means that positive and negative vortex lumps are shed at a high frequency which results in them being much closer. Beyond a distance $40D$ downstream, the vortex lumps have diffused into one another generating a laminar wake characterised by adjacent positive and negative vortex sheets. The intensity of the maximum vorticity in the

https://doi.org/10.1017/jfm.2011.77 Published online by Cambridge University Press

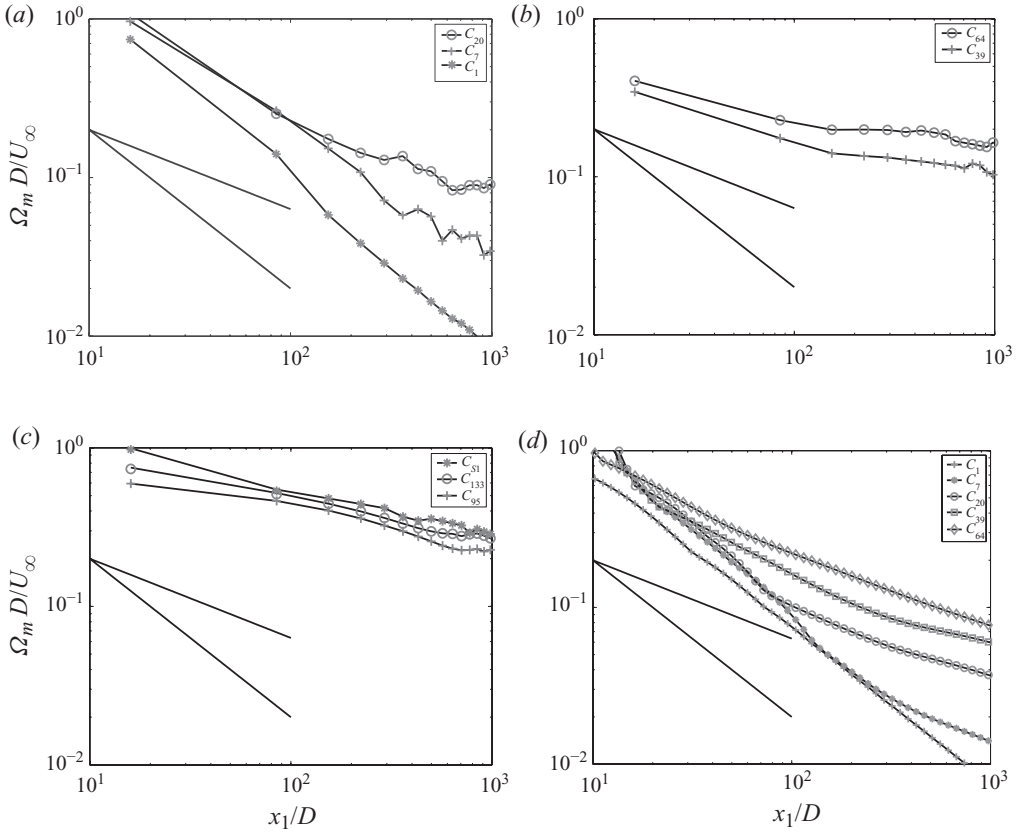

FIGURE 15. The variation of the maximum vorticity Ω_{max} with downstream distance is shown for (*a*) C_1, C_7 and C_{20}, (*b*) C_{39} and C_{64}, (*c*) C_{95}, C_{133} and C_{S1} and (*d*) model predictions for low fraction cases from (4.16). The two straight lines correspond to the decay laws $x_1^{-1/2}$ and x_1^{-1}.

sheets reduces at a rate of x_1^{-1} as a consequence of vorticity annihilation. Cases C_7 and C_{20} are similar with the maximum vorticity decaying as x_1^{-1} as a consequence of vorticity annihilation caused by wake intermingling, but beyond a distance of $250D$, vorticity can be seen to form into weak vortex lumps, whose maximum vorticity decays more slowly with time.

Both C_{39} and C_{64} (figure 15*b*) have a shear layer that separates from the shoulders of the array and continues downstream, until it becomes unstable and rolls up into a von Kármán vortex street. In the initial region, the stable shear layers are separated from one another. This prevents annihilation and means that there is only diffusive reduction from the shear layers, leading to a $x_1^{-1/2}$ decay in Ω_{max}. However, this decrease is considerably more rapid than for vortex lumps because the area over which diffusion occurs is much larger. At a distance downstream of $3D_G$ (C_{39}) or $5D_G$ (C_{64}), the rate of diffusion reduces as the vortex sheets roll up into more slowly diffusing discrete vortex lumps.

At high void fractions (C_{95} and C_{133}), the array of bodies alternately sheds large scale coherent vortices with positive and negative vorticity. The vortices are initially well separated (by a distance D_G) so that vorticity annihilation is negligible. The maximum magnitude of vorticity Ω_{max} decays slowly due to the vortex patches growing

https://doi.org/10.1017/jfm.2011.77 Published online by Cambridge University Press

in size by diffusion. The circulation of a vortex patch is defined as $\Gamma = \lambda \Omega_{max} \pi R_p^2$, where the vortex radius is R_p. Since Γ is conserved, and R_p^2 increases linearly due to diffusion, then $\Omega_{max} \sim \Gamma/\lambda(R_{p0}^2 + 2\nu x_1/U_\infty)$, where R_{p0} is the initial radius of the shed vortices. Far downstream, beyond a distance $x_1 \approx D_G^2 U_\infty/\nu \approx D_G Re_G$, the vortex patches intermingle when they have grown sufficiently large by diffusion that they can interact. Since the distance over which vorticity can diffuse (within a distance $x_1 < 1000D$) is much smaller than the initial size of the vortices, the decrease in the Ω_{max} is small in this region, as shown in figure 15(*c*).

When the flow is not dominated by vortex shedding from the array, the model assumptions become more appropriate and can account for the reduction of Ω_{max} through diffusion and annihilation (which are linear processes). Figure 15(*d*) shows the prediction of Ω_{max} from (4.16) for the low void fraction cases. The model predicts a rapid x_1^{-1} decay of Ω_{max} for C_1, C_7 and C_{20}, whose trend agrees with figure 15(*a*). The separation between the cylinders means that the model captures the shear layers ultimately generated for cases C_7–C_{64}, where Ω_{max} decreases as $x_1^{-1/2}$. The steady model cannot capture wake instabilities or when vortical lumps are created and is no longer appropriate far downstream for cases C_{39}–C_{64}.

6. Conclusion

In this paper, we have described a detailed numerical study of the effect of void fraction on two-dimensional flows past circular arrays of cylinders. Three distinct flow regimes have been identified:

(*a*) For low ϕ ($\phi < 0.05$), the flow interactions are weak within the array and force characteristics on each cylinder are similar to an isolated body. The wake of the group is composed of the identifiable individual wakes of the bodies making up the array. These rapidly dissipate through an annihilation process, as they are advected downstream, leading to a rapid decrease in the maximum vorticity.

(*b*) At moderate ϕ (between 0.05 and 0.15), a stable wake forms behind the array, which is stabilised by a bleed flow. The flow is locally steady and the lift force is negligible. Vorticity annihilation occurs between the cylinders. The maximum vorticity decays slowly with distance by the diffusive thickening of the attached shear layers. The shear layers become unstable some distance downstream and roll up to generate a vortex street.

(*c*) At high ϕ (> 0.15), the array begins to behave in a similar way to a solid cylinder. The signatures of the individual cylinders within the array are annihilated by wake interactions. The downstream flow consists of a vortex street where the maximum magnitude of vorticity decays slowly downstream.

To interpret the results of the numerical calculations, we developed a mathematical model which incorporates source and dipole contributions (from drag and inviscid blocking) and a wake model. The drag on the individual bodies within the array was estimated from the model. Predictions of mean drag coefficient, the distribution of mean forces within the array, the Eulerian mean average velocity and upstream velocity were compared with the numerical results. The comparison was reasonable for low void fractions. The model also shows that for localised groups of bodies, the mean flow within an array is dominated by the velocity deficit created by the wakes.

The numerical calculations give insight into the general processes that are common to many multibody flows. Previous discussions had focused on the effect of local strain in annihilating vorticity, for instance, in pipe bundles. We have applied a flow

https://doi.org/10.1017/jfm.2011.77 Published online by Cambridge University Press

diagnostic, commonly applied to turbulent flows, which has shown that the flow at the boundaries between body wakes becomes irrotational. This suggests that vorticity annihilation occurs largely through wake interactions.

A limitation in this work is the use of two-dimensional numerical calculations to model flows that are likely to become, to a degree, three-dimensional. For an individual body within the array, the Reynolds number characterising the flow is <100 as a result of the retarded free stream flow within the array. Given this, for an individual element in the array, the two-dimensional assumption based on the low Reynolds number provides a leading order description of the flow and force characteristics. However, while this Reynolds number is considerably less than required to generate a three-dimensional wake for an isolated element, early tripping arising from the complex array geometry cannot be anticipated.

The flow around the array, as a whole, will certainly have a three-dimensional component, as the Reynolds number is much greater than the typically accepted transition value of Reynolds number ≈ 190. Whilst the flow characteristics described above are still valid, it is likely that the array drag is then over predicted as a result of the two-dimension calculations. To understand these issues better, it will be necessary to study the three-dimensional flow through and around groups of bodies, where the additional effect of vortex stretching is likely to have an important dynamical effect on the flow. The main difficulty in doing this is that the computational size becomes a limiting factor.

This work has enabled a more developed appreciation of the characteristics of the flow field in multibody situations. Significant future developments can be expected with advances in modelling techniques and as greater computational resources become available.

We thank Dr Jeremy Yates and Clare Gryce for help with access to Legion and support in terms of resources. Department of Health funding for 'Transmission of pathogens in the healthcare environment: an intensive study of transmission by hand, cleaning materials and air to inform national policy on cleaning methodology and design of wards, equipment and furniture' during 2008-2010 (led by Dr Wilson, UCLH) provided partial support for A.N. during the completion of this paper.

Appendix

We describe the numerical formulation applied in this paper.

Step 1

The Navier–Stokes equation (2.1) was solved using a characteristic-based-split (CBS) algorithm based on the projection method of Chorin (1968), as described in Zienkiewicz & Codina (1995) and Zienkiewicz, Taylor & Nithiarasu (2005). In this method, an intermediate velocity field is introduced to uncouple the momentum and continuity equations; a characteristic method is used to stabilise the non self-adjoint operators in the CBS formulation which is written as

$$\frac{\tilde{\boldsymbol{u}} - \boldsymbol{u}^{(n)}}{\Delta t} = -\boldsymbol{u}^{(n)} \cdot \nabla \boldsymbol{u}^{(n)} + \nu \nabla^2 \boldsymbol{u}^{(n)} + \frac{1}{2} \Delta t \boldsymbol{u}^{(n)} \cdot \nabla \left(\boldsymbol{u}^{(n)} \cdot \nabla \boldsymbol{u}^{(n)} \right), \tag{A 1}$$

where $\tilde{\boldsymbol{u}}$ is the intermediate velocity field.

https://doi.org/10.1017/jfm.2011.77 Published online by Cambridge University Press

Step 2

Taking the divergence of the momentum equation and integrating from time t_n to $t_n + \Delta t$, gives

$$\Delta t \nabla^2 p^{(n)} = -\rho \nabla \cdot \tilde{\boldsymbol{u}}. \tag{A 2}$$

Step 3

The pressure calculated in Step 2 is used to correct the intermediate velocity so that it is solenoidal, resulting in

$$\boldsymbol{u}^{(n+1)} - \tilde{\boldsymbol{u}} = -\frac{\Delta t}{\rho} \nabla^2 p^{(n)}. \tag{A 3}$$

To solve the three-step problem, a set of basis functions $[\boldsymbol{N}] = [N_i, N_j, N_k]$ is introduced which depends on x_1 and x_2 and $\{\boldsymbol{u}_1\}$, $\{\boldsymbol{u}_2\}$ and $\{\boldsymbol{p}\}$ are 3×1 vectors of unknowns (e.g. $\{\boldsymbol{u}_1\} = [u_{1_i}, u_{1_j}, u_{1_k}]^{\mathrm{T}}$). In our formulation we applied linear basis functions. Within the triangular element, the velocity components and pressure are approximated by

$$u_i = [\boldsymbol{N}]\{\boldsymbol{u}_i\}, \quad \tilde{u}_i = [\boldsymbol{N}]\{\tilde{\boldsymbol{u}}_i\}, \quad p = [\boldsymbol{N}]\{\boldsymbol{p}\}, \tag{A 4}$$

for $i = 1, 2$. Here $\partial[\boldsymbol{N}]/\partial x_1 = \boldsymbol{b}/2A$ and $\partial[\boldsymbol{N}]/\partial x_2 = \boldsymbol{c}/2A$, where A is the area of the local element. Boundary conditions are imposed by row and column inserts into the global mass and diffusion matrices. The finite element method results in the following sets of equations, which were applied on an elemental basis.

Step 1

$$[\boldsymbol{M}]\frac{\{\tilde{\boldsymbol{u}}_i\} - \{\boldsymbol{u}_i\}^n}{\Delta t} = -[\boldsymbol{C}]\{\boldsymbol{u}_i\}^n - \nu[\boldsymbol{K}]\{\boldsymbol{u}_i\}^n - [\boldsymbol{K}_S]\{\boldsymbol{u}_i\}^n + \nu[\boldsymbol{F}]\{\boldsymbol{u}_i\}^n. \tag{A 5}$$

Step 2

$$[\boldsymbol{K}]\{\boldsymbol{p}\}^n = -\frac{\rho}{\Delta t}[[\boldsymbol{G}_1]\{\tilde{\boldsymbol{u}}_1\} + [\boldsymbol{G}_2]\{\tilde{\boldsymbol{u}}_2\}] + [\boldsymbol{F}]\{\boldsymbol{p}\}^n. \tag{A 6}$$

Step 3

$$[\boldsymbol{M}]\{\boldsymbol{u}_i\}^{n+1} = [\boldsymbol{M}]\{\tilde{\boldsymbol{u}}_i\} - \Delta t[\boldsymbol{G}_i]\{\boldsymbol{p}\}^n/\rho, \tag{A 7}$$

The local formulations on each element requires the evaluation of the following matrices and vectors:

$$[\boldsymbol{M}] = \frac{A}{12}\begin{bmatrix} 2 & 1 & 1 \\ 1 & 2 & 1 \\ 1 & 1 & 2 \end{bmatrix}, \quad [\boldsymbol{C}] = \frac{[\boldsymbol{M}]}{2A}\left(\{\boldsymbol{u}_1\}^n \boldsymbol{b} + \{\boldsymbol{u}_2\}^n \boldsymbol{c}\right), \tag{A 8}$$

$$[\boldsymbol{F}] = \frac{1}{2A}\int_{\Gamma_e}\left(\boldsymbol{N}^{\mathrm{T}} n_1 \,\mathrm{d}\Gamma \boldsymbol{b} + \int_{\Gamma_e} \boldsymbol{N}^{\mathrm{T}} n_2 \,\mathrm{d}\Gamma \boldsymbol{c}\right), \tag{A 9}$$

$$[\boldsymbol{K}_S] = \frac{[\boldsymbol{M}]\{\boldsymbol{u}_1\}\Delta t}{8A^2}\left[\{\boldsymbol{u}_1\}^{\mathrm{T}}\boldsymbol{b}^{\mathrm{T}}\boldsymbol{b} + \{\boldsymbol{u}_2\}^{\mathrm{T}}\boldsymbol{b}^{\mathrm{T}}\boldsymbol{c}\right] + \frac{[\boldsymbol{M}]\{\boldsymbol{u}_2\}\Delta t}{8A^2}\left[\{\boldsymbol{u}_1\}^{\mathrm{T}}\boldsymbol{c}^{\mathrm{T}}\boldsymbol{b} + \{\boldsymbol{u}_2\}^{\mathrm{T}}\boldsymbol{c}^{\mathrm{T}}\boldsymbol{c}\right]. \tag{A 10}$$

$$[\boldsymbol{K}] = \frac{1}{4A}\left[\boldsymbol{b}^{\mathrm{T}}\boldsymbol{b} + \boldsymbol{c}^{\mathrm{T}}\boldsymbol{c}\right], \quad [\boldsymbol{G}_1] = \frac{1}{6}\begin{bmatrix} 1 \\ 1 \\ 1 \end{bmatrix}\boldsymbol{b}, \quad [\boldsymbol{G}_2] = \frac{1}{6}\begin{bmatrix} 1 \\ 1 \\ 1 \end{bmatrix}\boldsymbol{c}. \tag{A 11}$$

https://doi.org/10.1017/jfm.2011.77 Published online by Cambridge University Press

To ensure numerical stability, the global time step must be shorter than minimum diffusive or advective times (on the size of the elements). Following Zienkiewicz *et al.* (2005, p. 112), the global time step was set as

$$\Delta t = \mathscr{S} \min\left(\frac{h_n}{u}, \frac{h_n^2}{\nu}\right), \tag{A 12}$$

where the safety factor is $\mathscr{S} = 0.5$. Here $u = \sqrt{u_1^2 + u_2^2}$ and h_n is a characteristic length-scale of a element, defined here as $h_n = \min(2 \times \text{element area/opposite side length})$ where the minimum is calculated over each side of the elements.

REFERENCES

Ball, D. J. & Hall, C. D. 1980 Drag of yawed pile groups at low Reynolds number. *ASCE J. R. Aero. Soc.* **90**, 128–38.

Batchelor, G. K. 1967 *An Introduction to Fluid Mechanics*. Cambridge University Press.

Bhattacharyya, S., Dhinakaran, S. & Khalili, A. 2006 Fluid motion around and through a porous cylinder. *Chem. Engng Sci.* **61**, 4451–4461.

Blackburn, H. M. 2006 Effect of blockage on critical parameters for flow past a circular cylinder. *Intl J. Numer. Meth. Fluids* **50**, 987–1001.

Castro, I. P. 1971 Wake characteristics of two-dimensional perforated plates normal to an air-stream. *J. Fluid Mech.* **46**, 599–609.

Chang, C. C., Yang, S. H. & Chu, C. C. 2008 A many-body force decomposition with applications to flow about bluff bodies. *J. Fluid Mech.* **600**, 95–104.

Chorin, A. J. 1968 Numerical solution of Navier–Stokes equations. *Math. Comput.* **22**, 745–762.

Codina, R., Coppola-Owen, H., Nithiarasu, P. & Liu, C.-B. 2006 Numerical comparison of CBS and SGS as stabilization techniques for the incompressible Navier–Stokes equations. *Intl J. Numer. Meth. Engng* **66**, 1672–1689.

Clift, R., Grace, J. & Weber, M. E. 1978 *Bubbles, Droplets and Particles*. Dover Publications. p. 381.

Davidson, P. A. 2004 *Turbulence: An Introduction for Scientists and Engineers*. Oxford University Press.

Eames, I., Hunt, J. C. R. & Belcher, S. E. 2004 Inviscid mean flow through and around groups of bodies. *J. Fluid Mech.* **515**, 371–389.

Eames, I., Roig, V., Hunt, J. C. R. & Belcher, S. E. 2007 Vorticity annihilation and inviscid blocking in multibody flows. *Nato Meeting Ukraine May* **69**.

Huang, Z., Kawall, J. G. & Keffer, J. F. 1996 Development of structure within the turbulent wake of a porous body. Part 2. Evolution of the three-dimensional features. *J. Fluid Mech.* **329**, 117–136.

Hunt, J. C. R. & Eames, I. 2002 The disappearance of laminar and turbulent wakes in complex flows. *J. Fluid Mech.* **457**, 111–132.

Hunt, J. C. R., Wray, A. A. & Moin, P. 1988 Eddies, stream and convergence zones in turbulent flows. In *Proc. 1988 Summer Program*, Stanford NASA. Centre for Turb. Res., CTR-S88.

Jeong, J. & Hussain, F. 2006 On the identification of a vortex. *Fluid Dyn. Res.* **28**, 449–464.

Kim, H.-B. & Lee, S.-J. 2001 Hole diameter effect on flow characteristics of wake behind porous fences having the same porosity. *J. Fluid Mech.* **285**, 69–94.

Legendre, D., Borée, J. & Magnaudet, J. 1998 Thermal and dynamic evolution of a spherical bubble moving steadily in a superheated or subcooled liquid. *Phys. Fluids* **10**, 1256.

Malan, A. G., Lewis, R. W. & Nithiarasu, P. 2002 An improved unsteady, unstructured, artificial compressibility, fnite volume scheme for viscous incompressible flows. Part II. Application. *Intl J. Numer. Meth. Engng* **54**, 715–729.

Moulinec, C., Hunt, J. C. R. & Nieuwstadt, F. T. M. 2004 Disappearing wakes and dispersion in numerically simulated flows through tube bundles. *Flow Turbul. Combust.* **73**, 95–116.

Nicolle, A. 2009 Flow through and around groups of bodies. PHD thesis, University College London.

https://doi.org/10.1017/jfm.2011.77 Published online by Cambridge University Press

Nithiarasu, P. & Zienkiewicz, O. C. 2005 Analysis of an explicit and matrix free fractional step method for incompressible flows. *Comput. Meth. Appl. Mech. Engng* **195**, 5537–5551.

Pearcey, H. H., Sing, S., Cash, R. F. & Matten, R. B. 1982 Interference effects on the drag loading for groups of cylinders in uni-directional flow. *Feltham UK Rep.* NMI R130.

Ramon, C. 2002 Stabilized finite element approximation of transient incompressible flows using orthogonal subscales. *Comput. Meth. Appl. Mech. Engng* **191**, 4295–4321.

Roig, V. & Tournemine, L. de 2007 Measurement of interstitial velocity of homogeneous bubbly flows at low to moderate void fraction. *J. Fluid Mech.* **572**, 87–110.

de Sampaio, P. A. B., Lyra, P. R. M., Morgan, K. & Weatherill, N. P. 1993 Petrov-Galerkin solutions of the incompressible Navier–Stokes equations in primitive variables with adaptive remeshing. *Comput. Meth. Appl. Mech. Engng* **106**, 143–178.

Singh, S. P. & Mittal, S. 2004 Flow past a cylinder: shear layer instability and drag crisis. *Intl J. Numer. Meth. Fluids* **47**, 75–98.

Taylor, P. H. 1991 Current blockage: reduced force on offshore space-frame structures. *Offshore Technol. Conf.* Paper no. OTC 6519.

Yu, P., Zeng, Y., Lee, T. S., Bai, H. X. & Low, H. T. 2010 Wake structure for flow past and through a porous square cylinder. *Intl J. Heat Fluid Flow* **31**, 141–153.

Zdravkovich, M. M. 1997 Flow around Circular Cylinders: Applications, vol 1. Oxford University Press.

Zienkiewicz, O. C. & Codina, R. 1995 A general algorithm for compressible and incompressible flow. Part I. The split, characteristic-based scheme. *Intl J. Numer. Meth. Fluids* **20**, 869–885.

Zienkiewicz, O. C., Taylor, R. L & Nithiarasu, P. 2005 *The Finite Element Method for Fluid Dynamics*, 6th edn. Elsevier Butterworth Heinemann.

https://doi.org/10.1017/jfm.2011.77 Published online by Cambridge University Press